Science Advances
AAAS

Supplementary Materials for

A modular strategy for distributed, embodied control of electronics-free soft robots

Qiguang He *et al.*

Corresponding author: Jordan R. Raney, raney@seas.upenn.edu

Sci. Adv. **9**, eade9247 (2023)
DOI: 10.1126/sciadv.ade9247

The PDF file includes:

Supplementary Text
Figs. S1 to S52
Legends for movies S1 to S10
References

Other Supplementary Material for this manuscript includes the following:

Movies S1 to S10

Discrete model

Here, we propose a discrete model to better understand the mechanics of the kirigami structures. A schematic of the discrete model is shown in Fig. S3. In the discrete model, each square (side length a) is considered to be a rigid body with mass M and moment of inertia J. Each square has three degrees of freedom: two translational displacements, u and v, and one rotational angle, θ. Note, θ_0 is the initial angle. Each hinge (connecting two squares) is modeled by three linear springs: a longitudinal spring with stiffness K_l, a shear spring with stiffness K_s, and a torsional spring with stiffness K_θ. Based on the discrete model, the equations of motion of a square at site (n, m) are

$$\begin{aligned}
M\frac{\partial^2 u_{n,m}}{\partial t^2} &= K_l\left(u_{n-1,m}+u_{n+1,m}-2u_{n,m}\right)+K_s(u_{n,m-1}+u_{n,m+1}-2u_{n,m})\\
&\quad+K_l\frac{a}{2\cos\theta_0}\left[\cos(\theta_{n-1,m}+\theta_0)-\cos(\theta_{n+1,m}+\theta_0)\right]\\
&\quad+(-1)^{n+m}K_s\frac{a}{2\cos\theta_0}\left[\sin(\theta_{n,m+1}+\theta_0)-\sin(\theta_{n,m-1}+\theta_0)\right]+F_u^{ext}
\end{aligned} \tag{1}$$

$$\begin{aligned}
M\frac{\partial^2 v_{n,m}}{\partial t^2} &= K_s(v_{n-1,m}+v_{n+1,m}-2v_{n,m})+K_l(v_{n,m-1}+v_{n,m+1}-2v_{n,m})\\
&\quad+K_l\frac{a}{2\cos\theta_0}\left[\cos(\theta_{n,m-1}+\theta_0)-\cos(\theta_{n,m+1}+\theta_0)\right]\\
&\quad+(-1)^{n+m}K_s\frac{a}{2\cos\theta_0}\left[-\sin(\theta_{n+1,m}+\theta_0)+\sin(\theta_{n-1,m}+\theta_0)\right]+F_v^{ext}
\end{aligned} \tag{2}$$

$$\begin{aligned}
J\frac{\partial^2 \theta_{n,m}}{\partial t^2} &= -K_\theta(\theta_{n-1,m}+\theta_{n+1,m}+\theta_{n,m+1}+\theta_{n,m-1}+4\theta_{n,m})\\
&\quad-K_l\frac{a}{2\cos\theta_0}\sin(\theta_{n,m}+\theta_0)\left(u_{n+1,m}+v_{n,m+1}-u_{n-1,m}-v_{n,m-1}\right)\\
&\quad-K_l\frac{a^2}{4\cos^2\theta_0}\sin(\theta_{n,m}+\theta_0)\left[\cos(\theta_{n+1,m}+\theta_0)-\cos(\theta_{n-1,m}+\theta_0)\right.\\
&\quad\left.-\cos(\theta_{n,m+1}+\theta_0)-\cos(\theta_{n,m-1}+\theta_0)-4\cos(\theta_{n,m}+\theta_0)+8\cos\theta_0\right]\\
&\quad+(-1)^{n+m}K_s\frac{a}{2\cos\theta_0}\cos(\theta_{n,m}+\theta_0)\left(u_{n,m+1}-u_{n,m-1}+v_{n-1,m}-v_{n+1,m}\right)\\
&\quad+K_s\frac{a^2}{4\cos^2\theta_0}\cos(\theta_{n,m}+\theta_0)\left[\sin(\theta_{n+1,m}+\theta_0)+\sin(\theta_{n,m+1}+\theta_0)\right.\\
&\quad\left.-4\sin(\theta_{n,m}+\theta_0)+\sin(\theta_{n-1,m}+\theta_0)+\sin(\theta_{n,m-1}+\theta_0)\right]+M^{ext}\,,
\end{aligned} \tag{3}$$

where F_u^{ext} and F_v^{ext} are the external forces along the x and y axes, respectively, and M^{ext} is the external moment.

To investigate the static behavior of the system, we remove the inertial terms on the left side of the governing equations. By introducing the normalized displacements $U = u/a$ and $V = v/a$, and stiffnesses $K_1 = K_s/K_l$ and $K_2 = K_\theta/(K_l a^2)$, we obtain the dimensionless governing equations of the $(n, m)^{th}$ square:

$$\begin{aligned}
0 &= (U_{n-1,m}+U_{n+1,m}-2U_{n,m})+K_1\left(U_{n,m-1}+U_{n,m+1}-2U_{n,m}\right)\\
&\quad+\frac{1}{2\cos\theta_0}\left[\cos(\theta_{n-1,m}+\theta_0)-\cos(\theta_{n+1,m}+\theta_0)\right]\\
&\quad+(-1)^{n+m}\frac{K_1}{2\cos\theta_0}\left[\sin(\theta_{n,m+1}+\theta_0)-\sin(\theta_{n,m-1}+\theta_0)\right]+\frac{F_u^{ext}}{K_l a}\\
&\quad\equiv \bar{F}_u^{int}+\bar{F}_u^{ext}
\end{aligned} \tag{4}$$

$$
\begin{aligned}
0 &= K_1(V_{n-1,m} + V_{n+1,m} - 2V_{n,m}) + (V_{n,m-1} + V_{n,m+1} - 2V_{n,m}) \\
&+ \frac{1}{2\cos\theta_0}\left[\cos(\theta_{n,m-1} + \theta_0) - \cos(\theta_{n,m+1} + \theta_0)\right] \\
&+ (-1)^{n+m}\frac{K_1}{2\cos\theta_0}\left[-\sin(\theta_{n+1,m} + \theta_0) + \sin(\theta_{n-1,m} + \theta_0)\right] + \frac{F_v^{ext}}{K_l a} \\
&\equiv \bar{F}_v^{int} + \bar{F}_v^{ext}
\end{aligned}
\tag{5}
$$

$$
\begin{aligned}
0 &= -K_2(\theta_{n-1,m} + \theta_{n+1,m} + \theta_{n,m+1} + \theta_{n,m-1} + 4\theta_{n,m}) \\
&- \frac{1}{2\cos\theta_0}\sin(\theta_{n,m} + \theta_0)\,(U_{n+1,m} + V_{n,m+1} - U_{n-1,m} - V_{n,m-1}) \\
&- \frac{1}{4\cos^2\theta_0}\sin(\theta_{n,m} + \theta_0)\left[\cos(\theta_{n+1,m} + \theta_0) - L\cos(\theta_{n-1,m} + \theta_0)\right. \\
&\left. - \cos(\theta_{n,m+1} + \theta_0) - \cos(\theta_{n,m-1} + \theta_0) - 4\cos(\theta_{n,m} + \theta_0) + 8\cos\theta_0\right] \\
&+ (-1)^{n+m}\frac{K_1}{2\cos\theta_0}\cos(\theta_{n,m} + \theta_0)\,(u_{n,m+1} - u_{n,m-1} + v_{n-1,m} - v_{n+1,m}) \\
&+ \frac{K_1}{4\cos^2\theta_0}\cos(\theta_{n,m} + \theta_0)\left[\sin(\theta_{n+1,m} + \theta_0) + \sin(\theta_{n,m+1} + \theta_0)\right. \\
&\left. -4\sin(\theta_{n,m} + \theta_0) + \sin(\theta_{n-1,m} + \theta_0) + \sin(\theta_{n,m-1} + \theta_0)\right] + \frac{M^{ext}}{K_l a^2} \\
&\equiv \bar{M}^{int} + \bar{M}^{ext},
\end{aligned}
\tag{6}
$$

The assembly of Eq. (4)-(6) for all (n, m) yields the dimensionless governing equation of the whole system

$$
\bar{\mathbf{F}}^{int}(\mathbf{u}) + \bar{\mathbf{F}}^{ext} = \mathbf{0} \tag{7}
$$

where $\bar{\mathbf{F}}^{int}(\mathbf{u})$ and $\bar{\mathbf{F}}^{ext}$ are two vectors obtained by assembling the normalized internal and external forces of all the squares in the system, respectively. Since $\mathbf{F}^{int}(\mathbf{u})$ nonlinearly depends on the displacement vector $\mathbf{u} = [u_1\, v_1\, \theta_1 \ldots u_N\, v_N\, \theta_N]^T$, we employ the Newton-Raphson method to numerically solve Eq. (7). To this end, we first define a function $\mathbf{G}(\mathbf{u}) = \mathbf{F}^{int}(\mathbf{u}) + \mathbf{F}^{ext}$. Then, the solution of Eq. (7) can be approximated using the following algorithm:

$$
\mathbf{u}_{j+1} = \mathbf{u}_j - \left[\nabla\mathbf{G}|_{\mathbf{u}_j}\right]^{-1}\mathbf{G}(\mathbf{u}_j) \tag{8}
$$

where $\nabla\mathbf{G}|_{\mathbf{u}_j}$ is the gradient of $\mathbf{G}$ evaluated at $\mathbf{u} = \mathbf{u}_j$, corresponding to the global stiffness matrix.

Static behavior of kirigami squares: a parametric study

We perform the following analysis to further reduce the number of design parameters for the actual kirigami body. From fundamental structural mechanics, the equivalent longitudinal, shear, and torsional springs of a thin hinge can be described invoking classical rod and cantilever beam models as follows

$$
\begin{aligned}
K_l &= EA/L_h \\
K_s &= 3EI/L_h^3 \\
K_\theta &= EI/L_h\ ,
\end{aligned}
\tag{9}
$$

where E is the the Young's modulus, L_h is the length of the hinge, and A and I are the area and second moment of area of the hinge's cross section, respectively. Considering a rectangular cross section with base b and height h, we have $A = bh$ and $I = bh^3/12$. Subsituting them into Eq. (9) and recalling the definition of K_1 and K_2, the two normalized stiffnesses can be rewritten as

$$\begin{aligned} K_1 &= h^2/(4L_h^2) \\ K_2 &= h^2/(12a^2)\ . \end{aligned} \tag{10}$$

Based on Eq. (10), the normalized stiffnesses are purely linked to the geometrical properties of the kirigami structure, including the length of the hinge L_h, the height of the hinge's cross section h, and the side length of the square a. This result indicates that the mechanical behavior of the kirigami structures can be tuned via a few geometrical properties. In the following, we will rely on the Newton-Raphson algorithm (i.e., Eq. (8)) to investigate the static deformation of kirigami structures, which will be exploited to provide useful guidelines for the design of the kirigami soft robot.

Tensile deformation

We now consider a kirigami structure consisting of 4×14 squares with $\theta_0 = \pi/4$ (i.e., initially closed), which is under tensile stretching as shown in Fig. S4A. The external forces $\bar{\mathbf{F}}$, remaining in the positive x direction, are applied to the two squares located in the last column and highlighted in green. Boundary conditions are imposed on the two squares located in the first column and highlighted in black, with degrees of freedom denoted as (U_1, V_1, θ_1) and (U_2, V_2, θ_2). Specifically, a boundary condition is imposed by setting $U_1 = V_1 = U_2 = 0$. The extension of the structure is defined as

$$\varepsilon = \frac{l - L}{L} \times 100\% \tag{11}$$

where l and L are the original and deformed lengths of the structure, respectively. In Figs. S4B-C, we plot the extension ε as functions of the normalized force $|\bar{\mathbf{F}}|$ for various pairs of the normalized stiffnesses (K_1, K_2). Specifically, we set $K_2 = 0.02$ and vary K_1 from 0.01 to 1 in Fig. S4B, while we set $K_1 = 0.2$ and vary K_2 from 0.01 to 0.05 in Fig. S4C. From a visual inspection, we observe that, under the same loading conditions, ε increases significantly as K_2 decreases. However, ε varies much less in response to the change in K_1, especially when K_1 is in the range of $[0.1, 0.5]$ (a realistic range to achieve in experiments). As a result, if our goal is to maximize the extension, we need to set K_2 as low as possible, which implies a short height of the hinge cross section h and a large side length of the square a.

Mechanical constraint-driven steering deformation

We now introduce two mechanical constraints in the structure, which are located at the center of the bottom row and highlighted in red, as shown in Fig. S5A. The "Mechanical constraints" refers to the local constraints provided by responsive materials that locally inhibit the opening of the kirigami squares, causing the kirigami to bend. In the simulation, the torsional stiffness of the hinge connecting the two mechanical constraints are set to a very high value, i.e., 1000 times larger than the torsional stiffness of the other hinges. This effectively prevents the rotation of the squares associated with the mechanical constraints. We consider the same boundary conditions, but the external force $\bar{\mathbf{F}}$ is allowed to change its direction during deformation. For simplicity, we introduce a single parameter λ to control the direction of $\bar{\mathbf{F}}$, which relates α to γ by a linear relation: $\gamma = \lambda\alpha$, where α is the angle between the horizontal line and a line perpendicular to the deformed last column (denoted as $\mathbf{n}$), and γ is the angle between $\bar{\mathbf{F}}$ and $\mathbf{n}$. Clearly, $\lambda = 0$ corresponds to the case where $\bar{\mathbf{F}}$ remains horizontal, and $\lambda = 0$ corresponds to the case where $\bar{\mathbf{F}}$ is always perpendicular to the last column during deformation. We also define α as the steering angle of the structure. In Fig. S5B-C, we show the effects of three different parameters (K_1,K_2,γ) on the steering angle α. We observe that α increases dramatically as K_2 and γ decrease, while it is less affected by K_1. As a result, if our primary goal is to achieve large steering angles for a given γ, we need to design the kirigami body with a small K_2, which again implies a short height of the hinge cross section h and a large side length of the square a.

Finite element results

We conducted finite element analysis using ABAQUS to understand the bending of the robots when subjected to an inflated pneumatic actuator. Numerical simulations were conducted with ABAQUS static analysis with a symmetric model with respect to the plane parallel to the kirigami layer.

First, we set up a model with a half tube simulating the behavior of the pneumatic actuator. We modeled a capped cylindrical tube with wall thicknesses using the same parameters in the experiments. The wall of the tube is modeled as an HGO hyperelastic anisotropic material which is used to model similar actuators in previous work (66). The strain energy density of HGO materials is defined as:

$$W = C_{10}(I_1 - 3) + \frac{k_1}{2k_2}\left[\exp\left[k_2(I_4 - 1)^2\right] - 1\right] \tag{12}$$

where I_1 is the first invariant of a given deformation gradient $\mathbf{F}$ and I_4 is the forth invariant with respect to a fiber direction $\mathbf{a}$. I_4 can be computed using the Cauchy-Green tensor $C = \mathbf{F}\mathbf{F}^T$:

$$I_4 = \mathbf{a} \cdot (\mathbf{C} \cdot \mathbf{a}) \tag{13}$$

C_{10}, k_1, and k_2 are fitting parameters for the model with k_2 having very little impact on the results of the fitting and is taken as $k_2 = 0.01$. Here, C_{10} represents the modulus of the matrix material, which in our pneumatic actuator is just a silicone rubber, while k_1 represents the degree of anisotropy, which arises due to the fibers (kevlar). The parameters for the pneumatic actuator are calibrated by comparing the extension of the actuator under various applied pressures, using both simulations and experiments. As shown in Fig. S6A, the best fit uses parameters $C_10 = 14$ kPa and $k_1 = 350$ kPa. Note, the value for C_10 is consistent with previous reported values for Ecoflex 30 using a hyperelastic material model. In Fig. S6B, we place the actuated tube at the indicated pressure in the finite element model together with the experimental images to compare their length.

The two ends of the pneumatic actuator are rigidly constrained to a kirigami layer comprising rotating squares. In Fig. S6, we show the finite element results of the robot inflating as pressure is applied. Here the kirigami layer is modeled as neo-Hookean material with one fitting parameter, C_{10}. Since the silicone rubber for the kirigami layer is different from the pneumatic actuator, we need to recalibrate the material constant for the kirigami layer. To do so, we extract the extension of the entire robot in both experiments and simulations and find the best fit is achieved using $C_{10} = 20$ kPa. Using these parameters, the FEA matches experimental data well, as shown in Fig. S6C. In Fig. S6D, we compare experimental images of the robot FEA results at indicated pressures. The finite element analysis is seen to match the deformation of the entire robot accurately.

After calibrating the material parameters for each component of the robot, control modules are simulated as mechanical constraints in the FEA as rigid plates restricting rotation of various squares, similar to experiments. A rigid plate (E=10 GPa) is placed in rigid contact with the squares that are restricted. We also place vertical columns under the kirigami layer (same as experiments). Friction between the pneumatic actuator and the columns are defined using hard contact and standard Coulomb friction. The contact and friction from the columns constrain the pneumatic actuator close to the center line of the actuated kirigami layer, representing the bending behavior of the entire robot under mechanical constraints. Fig. S8A shows snapshots of both experimental and FEA data under the same applied pressure (15 kPa). Fig. S8B shows that the bending angle predicted by FEA agrees closely with experiments up to 15 kPa. After 15 kPa, there is significant contact and deformation in the finite element model and convergence becomes difficult in the static model. Experiments and FEA are shown in Fig. S8C and D.

Kirigami design considerations

The kirigami robot body can be constructed of any number of squares along its length (N_L) and width (N_w). The initial angle of opening of the squares θ_{lin} and the hinge thickness t also influence the mechanical response of the system. During actuation, the pneumatic actuator extends, forcing the squares in the kirigami to rotate and open. This opening consists of two stages: The first stage is rotation dominated. The extension of the kirigami can be found as (56):

$$\delta = 2l(\cos\theta - \cos(\theta_{lin} - \theta)) \tag{14}$$

with each square in the system being rotated by θ.

In a system with $N_w \times N_L$ squares (as illustrated in Fig. S7A), the initial width and length of the robot are:

$$w = (N_w - 1)2l\cos\theta_{lin} \tag{15}$$

$$L_1 = L_2 = (N_L - 1)2l\cos\theta_{lin} \tag{16}$$

When a mechanical constraint with a size of N_d is inserted in the robot, it constricts the rotation of $N_d - 1$ squares along one edge during opening of the kirigami layer. As illustrated in Fig. S7B, for a prescribed rotation of all other squares in the system, the width w', length of the side with the mechanical constraint L_1', and length of the side without the mechanical constraint N_2' can be found as:

$$w' = (N_w - 1)2l\cos(\theta_{lin} - \theta) \tag{17}$$

$$L_1' = (N_L - N_d - 2)2l\cos(\theta_{lin} - \theta) + (N_d - 1)2l\cos\theta_{lin} \tag{18}$$

$$L_2' = (N_L - 1)2l\cos(\theta_{lin} - \theta) \tag{19}$$

By observing both experimental images and numerical simulations (Fig. S8A and B), the robots when bent can be approximated as an annular sector. With this assumption, we derive the bending angle α as:

$$\alpha = \frac{L'_2 - L'_1}{w'} = \frac{N_d - 1}{N_w - 1} \frac{\cos(\theta_{lin} - \theta) - \cos\theta_{lin}}{\cos(\theta_{lin} - \theta)}$$
$$\alpha = \frac{N_d - 1}{N_w - 1}(1 - \frac{1}{\lambda}) \tag{20}$$

The extension λ of the kirigami is related to the rotation of the squares θ (56):

$$\lambda = \frac{\cos(\theta_{lin} - \theta)}{\cos\theta_{lin}} \tag{21}$$

We plot the prediction using the annular sector model of bending angle with various lengths of mechanical constraints as shown in Fig. S7 and S8. The experimental results are shown in Fig. S11. Our model can quantitatively predict the bending angle at low pressure for different constraint sizes, and qualitatively describe the effect of other geometric parameters.

In order to maximize the bending angle of the robot, the robot should minimize the number of squares in the width direction N_w, maximize the number of mechanical constraints along an edge, and maximize the extension of the robot. In the experiment, we fabricate kirigami squares with three different sizes (4×10, 4×14, 6×14). We attach rigid mechanical constraints, which mechanically constrain the rotation and opening of the kirigami platforms (Fig. S12). In practice, the minimum number of squares we can have along the width of the robot is 4, in order to attach the pneumatic actuator to the kirigami robot. The experimental results show that the kirigami with a size of 4×14 can generate the largest bending angles (Fig. S12). We therefore choose these dimensions for the robot. It is also worth noting that the number of squares in the length direction, N_L, has little effect on the bending angle (Fig. S13).

The last consideration is to maximize the strain. For the rotating square system, the force-displacement curve has two distinct region: an initial rotation-dominated region and later an extension-dominated region. The force increases drastically in the extension region. During both experiments and numerical simulations, we observe buckling of the pneumatic actuator at larger air pressures. This buckling behavior is undesired, since the robot should walk straight when no mechanical constraints are present. However, limiting the actuation to lower air pressure means less extension of the robot is achieved each actuation cycle, providing less bending with mechanical constraints. To maximize the extension and bending of each cycle, the parameters of the kirigami are chosen to maximize the strain at which the deformation transitions from rotation dominated to extension dominated. In order to maximize the critical strain, the initial rotation of the rotating squares needs to be minimized (θ_{lin} being close to zero) and the hinge thickness needs to be as small as possible (56). In this work, θ_{lin} is chosen to be 5° to make molding of the rotating squares possible. We also confirm the effect of the hinge thickness by testing two samples with hinge thickness of 1.0 mm and 1.7 mm. The force-strain curves of the two samples are measured using a universal testing machine as shown in Fig. S10. The system with smaller hinge thickness has a much larger critical strain: The critical strains for the two samples with hinge thickness of 1.0 mm and 1.7 mm are 27% and 12.5%, respectively.

Effect of the length of LCE strips in the control modules

For the control module (integrated with CNT-LCE) shown in Fig. 3C, which enables the robot to steer closer to stimuli, the length of the CNT-LCE strip is a critical parameter.

When no external stimuli (heat or light) are present, the square units can freely rotate and open (e.g., room temperature). The CNT-LCE strip should not constrain the rotating and opening of the squares. However, when the control module is subjected to the stimuli (e.g., high temperature), the CNT-LCE strip contracts, and the contractile force should constrain the rotation of the squares, causing the kirigami body to bend. In the experiments, we design CNT-LCE strips with three lengths, 35 mm, 45 mm, and 55 mm (Fig. S21). The force-strain relationship of the square units (integrated with a CNT-LCE strip) is measured at different temperatures from 24°C to 145°C. As shown in Fig. S21B, at room temperature (24°C), the square units with a 35 mm length CNT-LCE strip are undesirably constrained. The 35 mm length is too short for this type of control module. In contrast, even at high temperatures (e.g., 145°C), the 55 mm CNT-LCE strip cannot generate a sufficient constraint on the motion of the squares (Fig. S21C). We therefore select the CNT-LCE strip with 45 mm length (Fig. S21D), which appropriately generates mechanical constraints at high temperatures but not at low temperatures. Similarly, for the control module that causes the robot to steer away from external stimuli (Fig. 3D), we choose the LCE strip with 45 mm length (Fig. S23).

Operational principle of the mechanical bistable valve

The operating principle of the bistable valve is shown in Fig. 7A. In the initial state, the membrane blocks the air tube inside the top chamber, preventing the flow of air. As a result, the pressurized air flows into the pneumatic actuator, causing it to extend. The pressure in the top chamber gradually increases. When the pressure in the top chamber reaches the critical value P_c, the membrane snaps. When this occurs, the air in the tube is no longer blocked, enabling it to flow out of the device and into the atmosphere. The pneumatic actuator therefore deflates. The pressure of the actuator versus time (measured experimentally) is plotted in Fig. 7B, showing the desired periodic pressure variation in the actuator. Note, the minimum pressure is 12 kPa, because a small amount of air is still pumped into the actuator during the deflation process. The elongation of the robot at this pressure is small (< 10 %).

Fluid control system

In some of the experiments (e.g., the pressure-extension measurements of Fig. 3), it is important to precisely control the pressure of the pneumatic actuator as a function of time. For this purpose, a customized fluid control system was built (Fig. S9), following the design of Ref. (67). The system includes a microcontroller (Arduino Mega 2560), solenoid valves and manifold, compact air pump, pressure sensors, MOSFET (metal oxide semiconductor field-effect transistor), power regulators, switches, and a linear potentiometer. The pressurized air is generated by the air pump, regulated via pulse-width modulation (PWM), and measured by the pressure sensors. For the static experiments (measurement of the extension of actuator and the bending angle of the kirigami body), the fluid control system is used manually (i.e., the air pressure is changed via the linear potentiometer).

Total cost of the soft autonomous robot

The estimation of the cost is based on the weight of each component of the soft robot and other costs (tube fitting, rods, pin etc). We use 190 g silicone rubber, 40 g R11, 10 g LCE. The total cost of the robot is approximately 50 dollars.

Figures

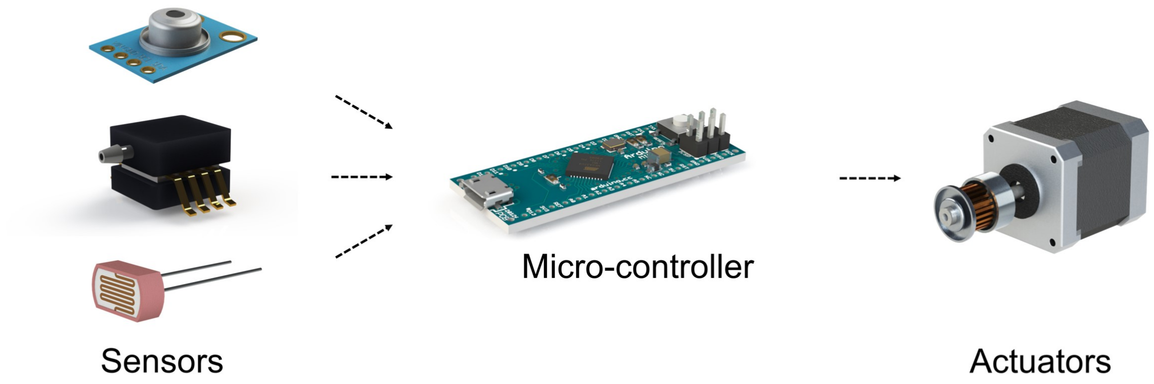

Figure S1: **The conventional sensing, control and actuation feedback loop.** In order to sense and respond to the environment, most robots use multiple traditional mechatronic devices that can be rigid, bulky, expensive and incompatible with soft materials.

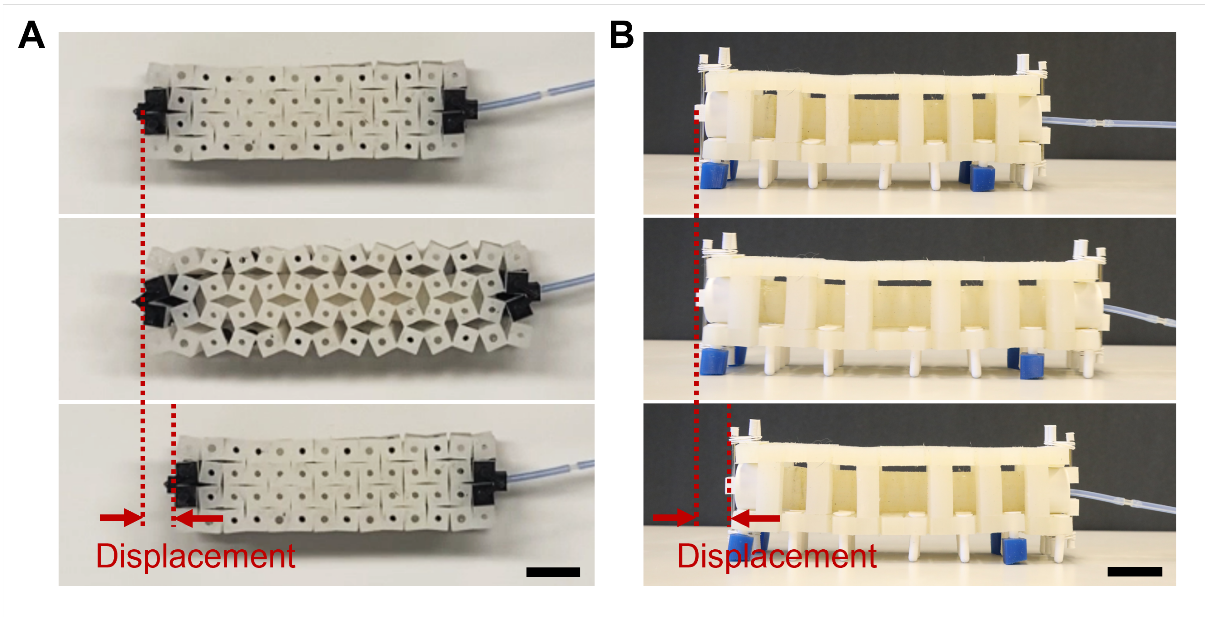

Figure S2: **The feet underneath the robot enable it to move forward due to anisotropic friction between the ground and robot.** When the pneumatic actuator is inflated, the rear feet act as stationary points and the front of the robot moves forward. Once the pneumatic actuator is deflated, the front feet are stationary, pulling the entire body forward. A displacement (of approximately 1 cm) can be generated after one cycle. Scale bar: 2 cm.

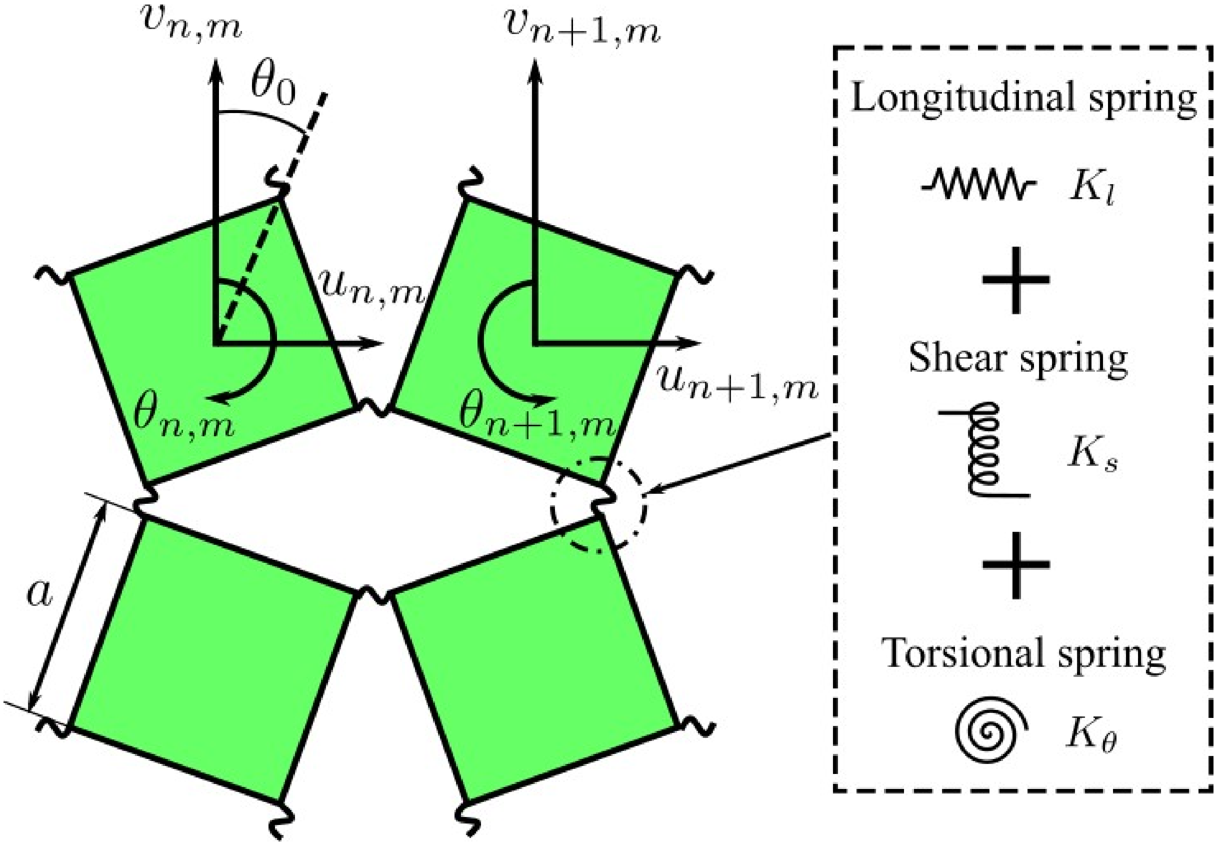

Figure S3: **Schematic for discrete model.** Each hinge connecting two squares is modeled by three linear springs: a longitudinal spring, a shear spring, and a torsional spring.

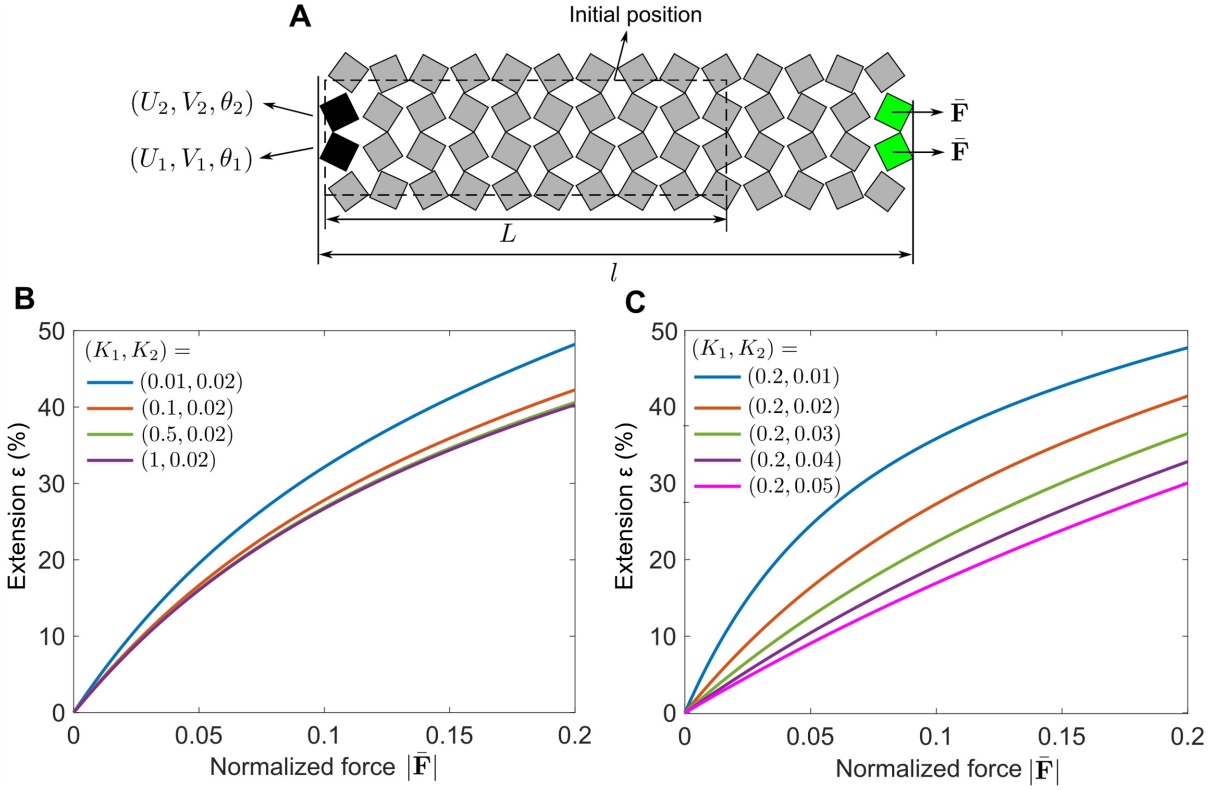

Figure S4: **Effects of K_1 and K_2 on the tensile deformation of a kirigami structure.** **A.** Schematic of a 4 × 14 kirigami under tensile deformation (the dashed box indicates the initial position of the kirigami). Boundary condition $U_1 = V_1 = U_2 = 0$ is applied to the squares in black, and horizontal forces $\bar{\mathbf{F}}$ are applied to the squares in green. **B.** Extension ε of the kirigami as functions of the normalized force $|\bar{\mathbf{F}}|$ against different values of K_1 with $K_2 = 0.02$. **C.** Extension ε of the kirigami as functions of the normalized force $|\bar{\mathbf{F}}|$ against different values of K_2 with $K_1 = 0.2$.

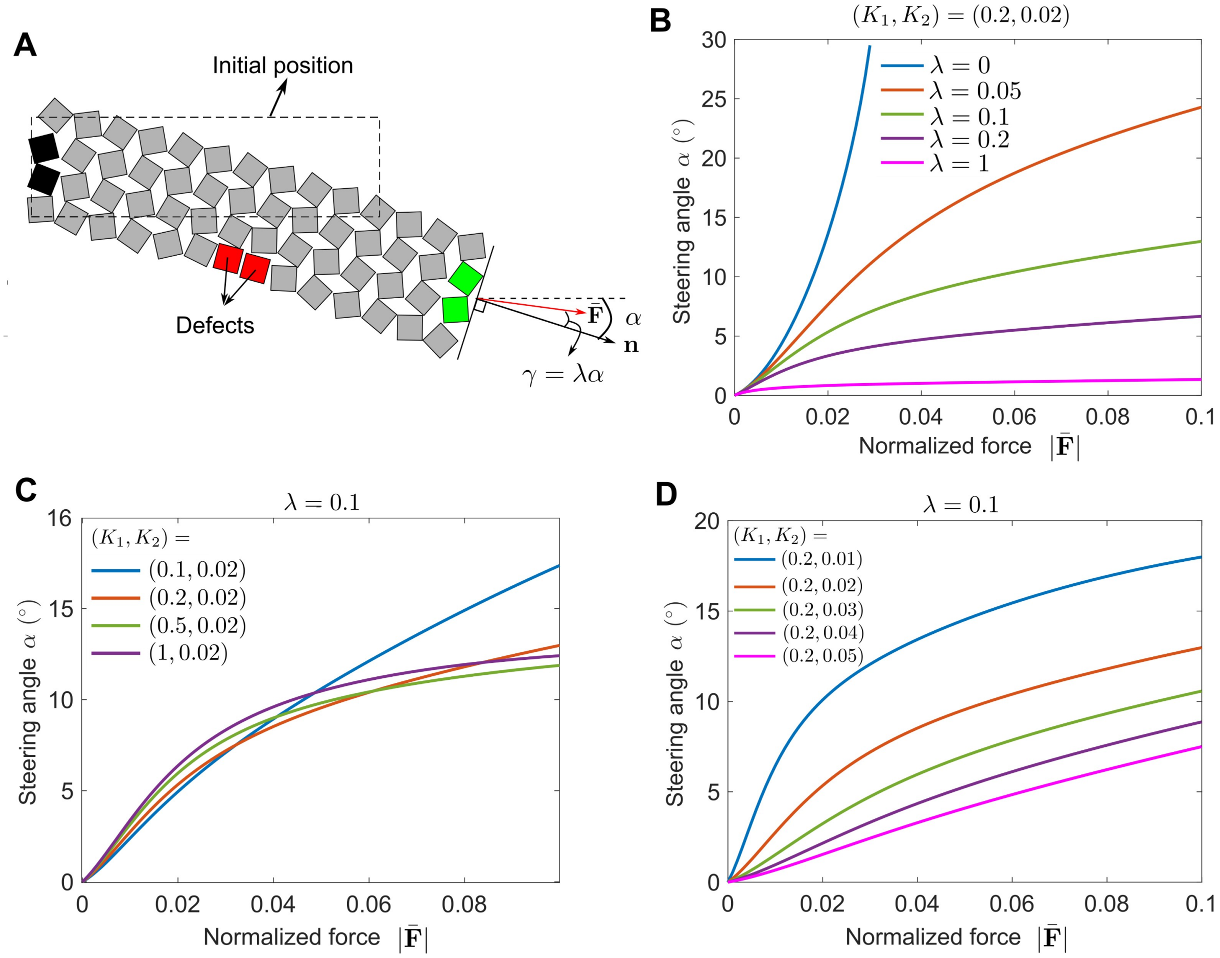

Figure S5: **Effects of γ, K_1, and K_2 on the steering deformation of a kirigami structure embedded with mechanical constraints.** **A.** Schematic of a 4×14 kirigami structure under constraint-driven steering. The two mechanical constraints highlighted in red are located at the center of the bottom row. The external force $\bar{\mathbf{F}}$ is allowed to change its direction during steering deformation, and the degree of the direction change is controlled by γ. **B.** Steering angles α of the kirigami as functions of the normalized force $|\bar{\mathbf{F}}|$ against different values of γ with $(K_1, K_2) = (0.2, 0.02)$. **C.** Steering angles α of the kirigami as functions of the normalized force $|\bar{\mathbf{F}}|$ against different values of K_1 with $\gamma = 0.1$ and $K_2 = 0.02$. **D.** Steering angles α of the kirigami as functions of the normalized force $|\bar{\mathbf{F}}|$ against different values of K_2 with $\gamma = 0.1$ and $K_1 = 0.2$.

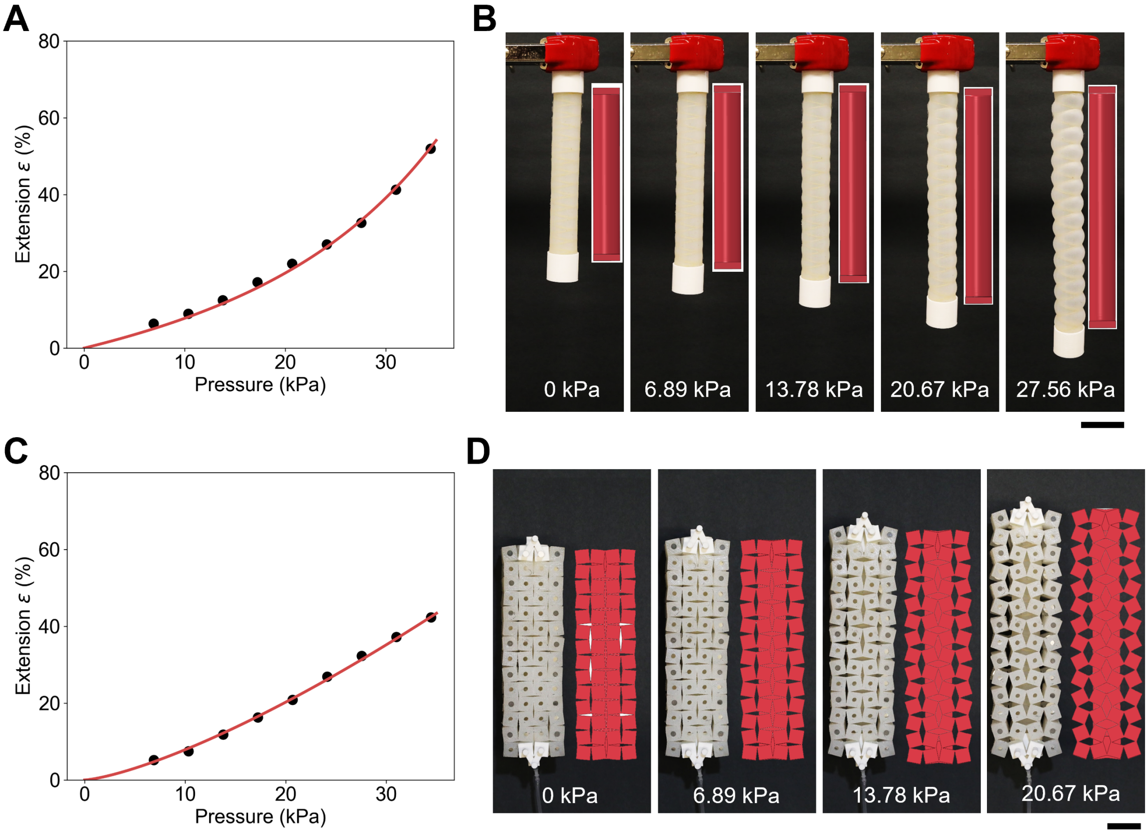

Figure S6: **Calibration of the parameters used in FEA. A.** Extension of pneumatic actuator as a function of pressure for both experiments (points) and finite element analysis (solid curves). Parameters for the pneumatic actuator are as follows: $C_{10} = 14$ kPa, $k_1 = 350$ kPa. **B.** Comparison of the pneumatic actuator as measured experimentally (white) and simulated via FEA (red). **C.** Extension of robot (including pneumatic actuator and kirigami layer) under various applied pressures for both experiments (points) and FEA (solid curves). Parameters for the kirigami are as follows: $C_{10} = 20$ kPa. **D.** Comparison of the actuated robot as measured experimentally (white) and via FEA (red). Scale bar in **B** and **D**: 2 cm.

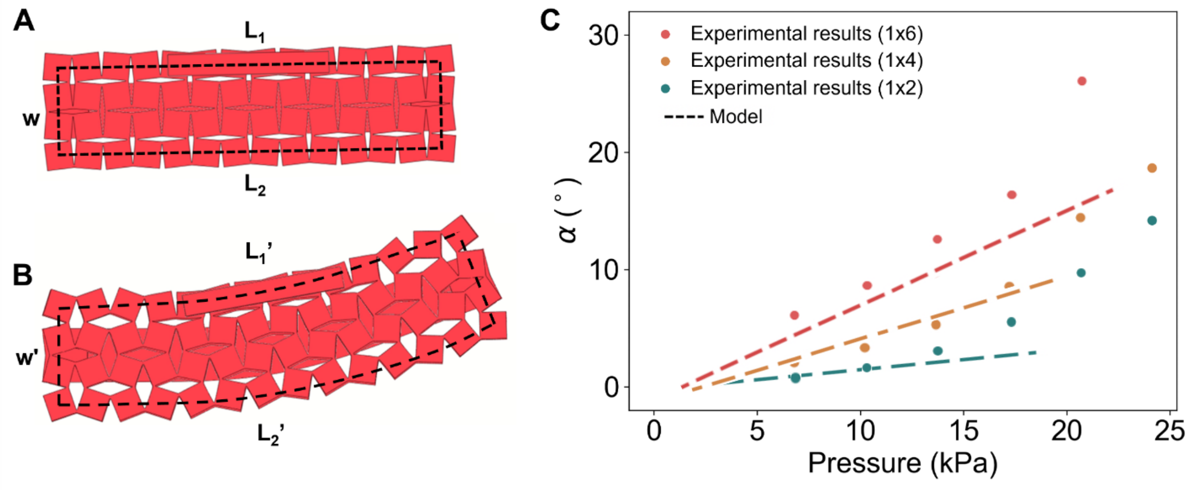

Figure S7: **Simplified geometric model for predicting actuating bending angle.** **A** Illustration of geometric parameters of unactuated robot. **B** Illustration after actuation. **C** Prediction of bending angle for robots with single constraint of various lengths via FEA (dash lines) shows consistency with experimental results (dots)..

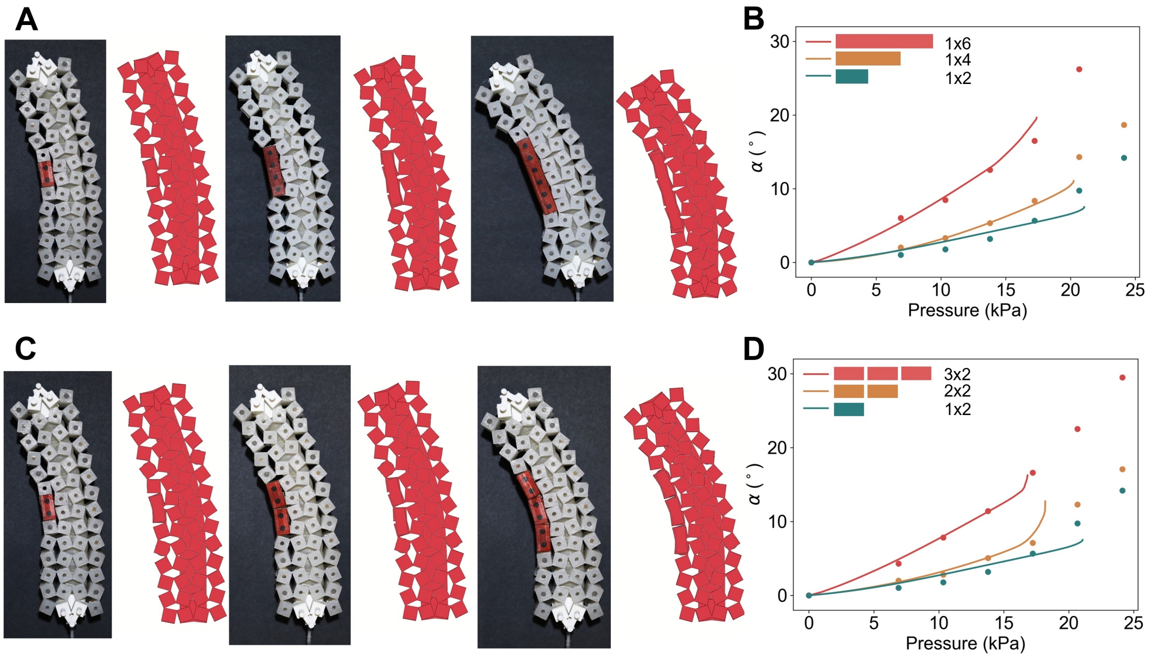

Figure S8: **FEA of robot with rigid mechanical constraints.** **A** The actuated robot with one mechanical constraint of various lengths, showing experiments (optical images) and FEA (in red). **B** Bending angle of the robot as a function of pressure for both experiments (points) and FEA (solid curves). **C-D** Same data as in A-B, but now multiple adjacent mechanical constraints are used (instead of the monolithic mechanical constraints of A-B).

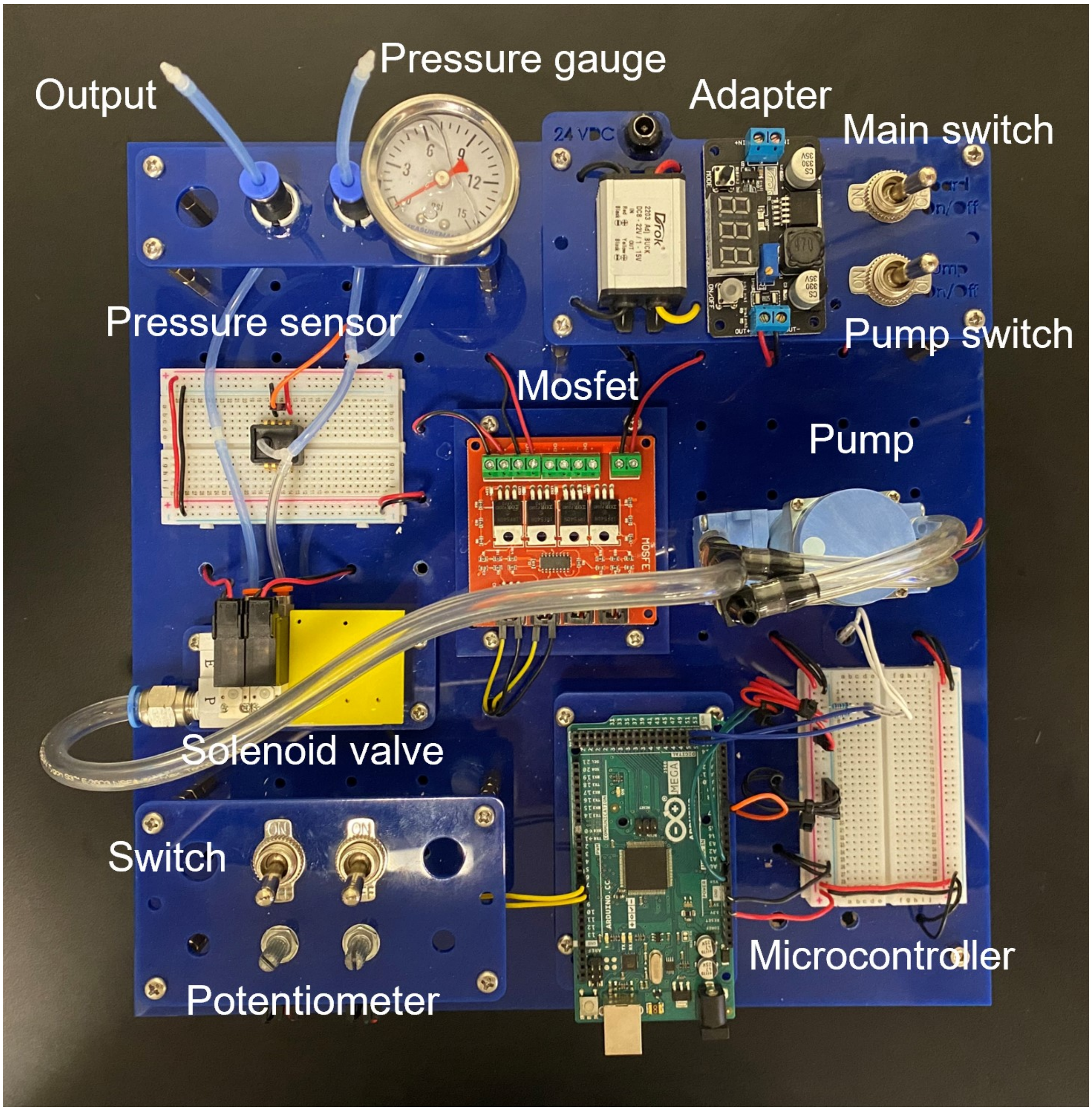

Figure S9: **A custom fluid control system.** This system consists of an air pump, microcontroller, solenoid valve, switches, potentiometers, MOSFET, pressure sensors, pressure gauge, and power adapters. The pressurized air can be generated by the air pump, regulated by the solenoid valve through pulse width modulation, and measured by the pressure sensors and pressure gauge.

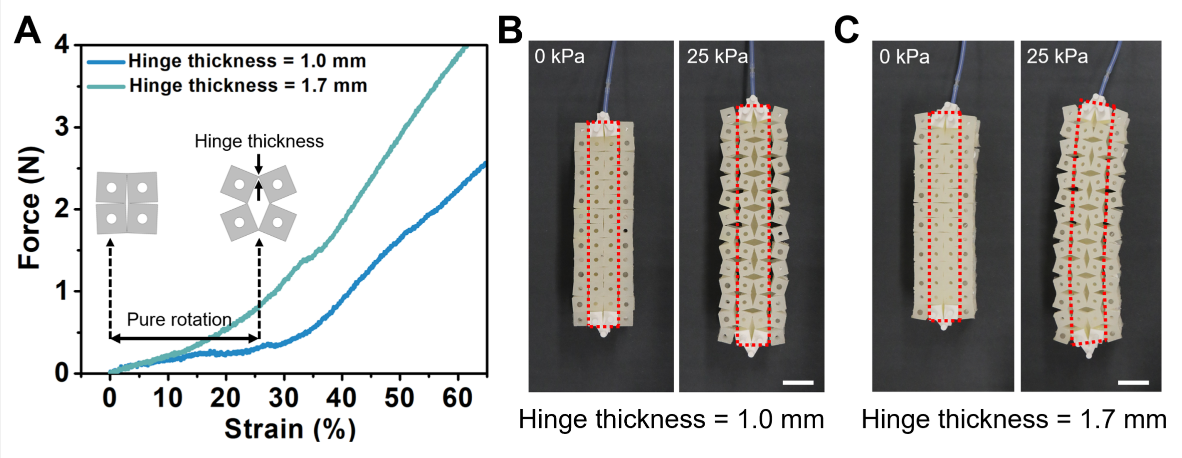

Figure S10: **The effect of the hinge thickness of the kirigami.** **A**: We measure the force-strain relationship of the kirigami platform with different hinge thicknesses (1.0 mm and 1.7 mm). The force is initially small, since the extension of the kirigami is initially rotation dominated. Later, at the “critical strain”, the extension becomes stretch-dominated. The smaller hinge thickness (1.0 mm) gives a larger critical strain. **B**: The kirigmai (1.0 mm hinge thickness) extends when the pneumatic actuator is inflated. **C**: The kirigami (1.7 mm hinge thickness) bends when the pneumatic actuator is inflated. This is due to buckling of the pneumatic actuator. Scale bar in **B** and **C**: 2 cm.

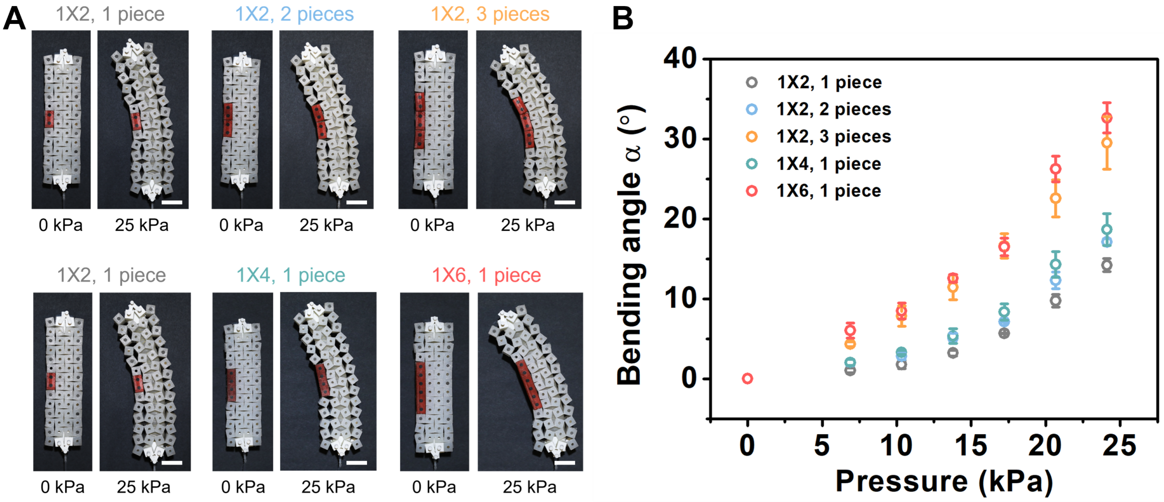

Figure S11: **The bending angle of the kirigami when using different types of mechanical constraints.** **A.** Optical images and **B.** bending angle (α) vs. pressure measurements, which show the effect of different sizes and types of mechanical constraints on the bending angle. Scale bar in **A**: 2 cm.

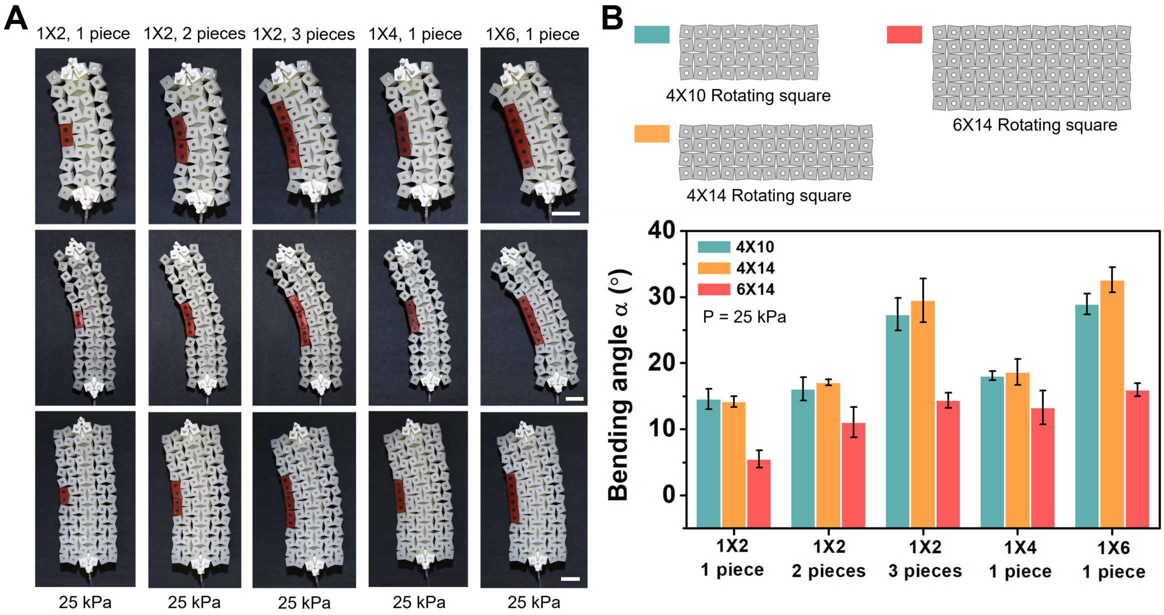

Figure S12: **The effect of the geometry of the kirigami.** In the experiments, three kirigami designs with different geometries (4x10, 4x14, 6x14) are tested. Multiple types of rigid mechanical constraints are attached to the kirigami body. The bending angle of the kirigami is measured. **A.** Experimental images of the kirigami after inflation of the pneumatic actuator to a pressure of 25 kPa. **B.** The bending angle α of the kirigami as a function of pressure. The 4×14 design of the kirigami can generate the largest bending angle. Scale bar in **A**: 2 cm.

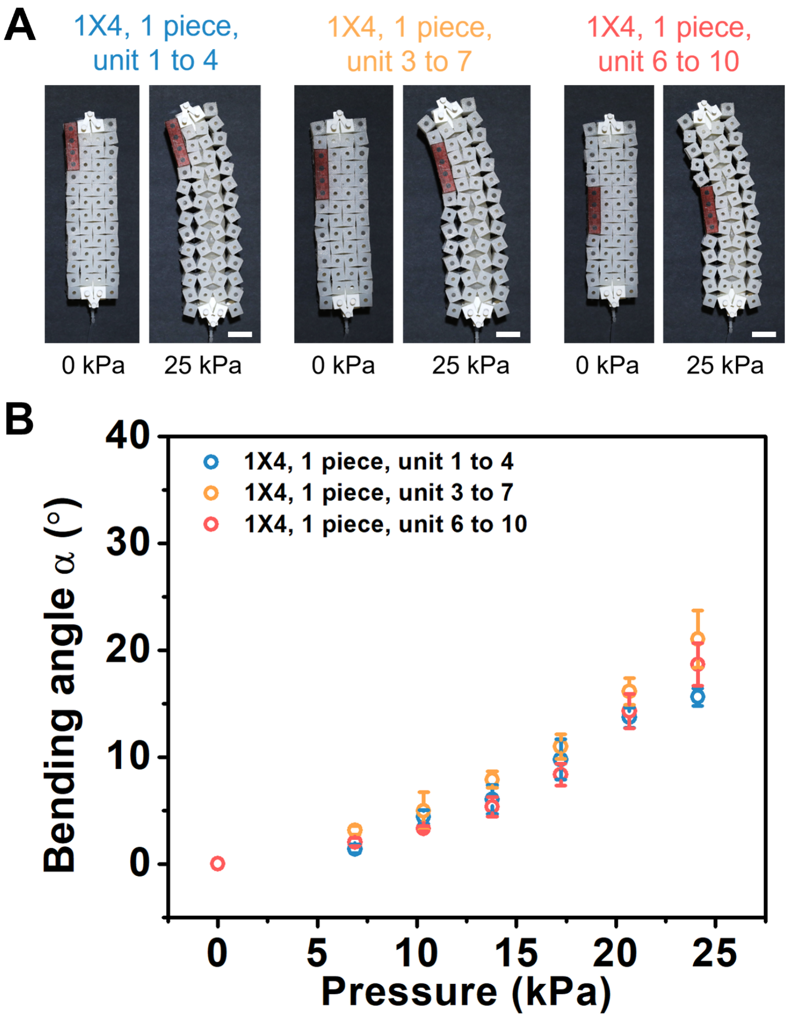

Figure S13: **The bending of the kirigami as a function of the location of rigid mechanical constraints.** A 1x4 rigid mechanical constraint is placed at different locations. The bending angle is measured after the pneumatic actuator is pressurized to 25 kPa. Scale bar in **A**: 2 cm.

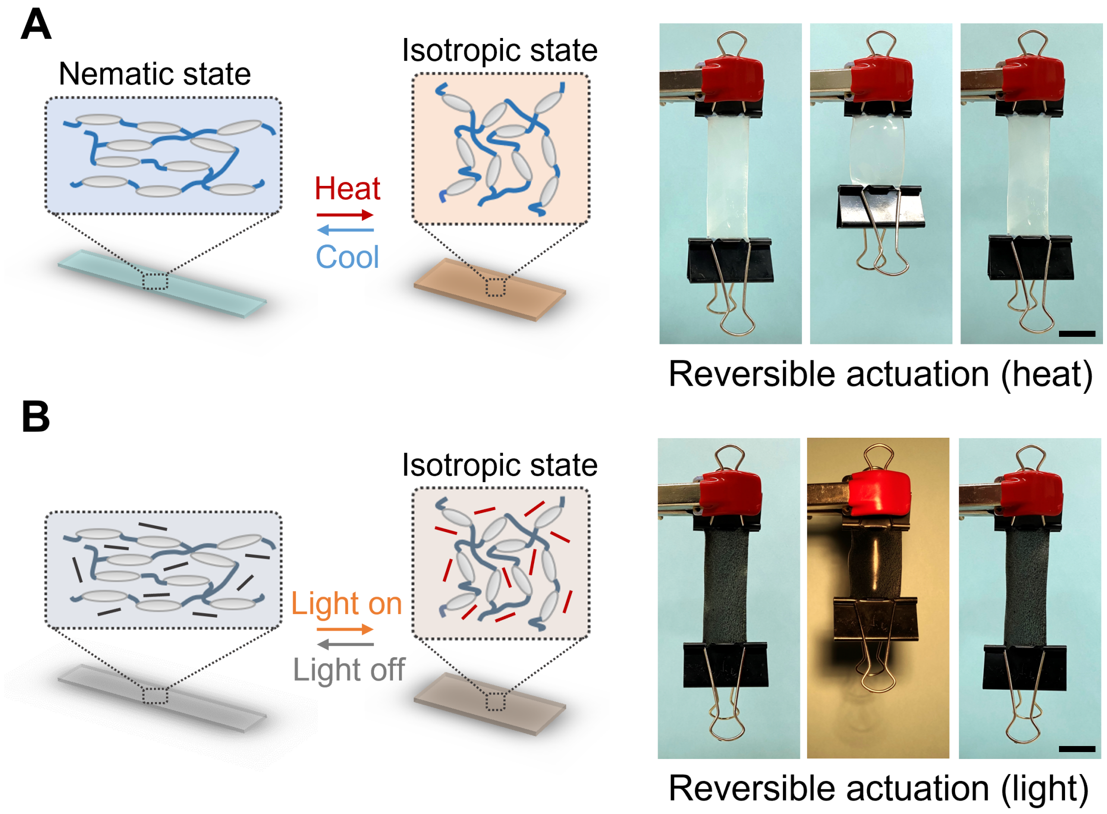

Figure S14: **Reversible actuation of LCEs and CNT-LCE composites. A.** When the LCE film is heated, it can contract due to a nematic-isotropic phase transition. The LCE can fully recover to its initial shape after cooling. **B.** When the CNT-LCE film is subjected to intense light, the CNT-LCE composite contracts due to the photothermal effect. The actuation is reversible: the CNT-LCE fully recovers when the light is switched off. Scale bar in **A** and **B**: 2 cm.

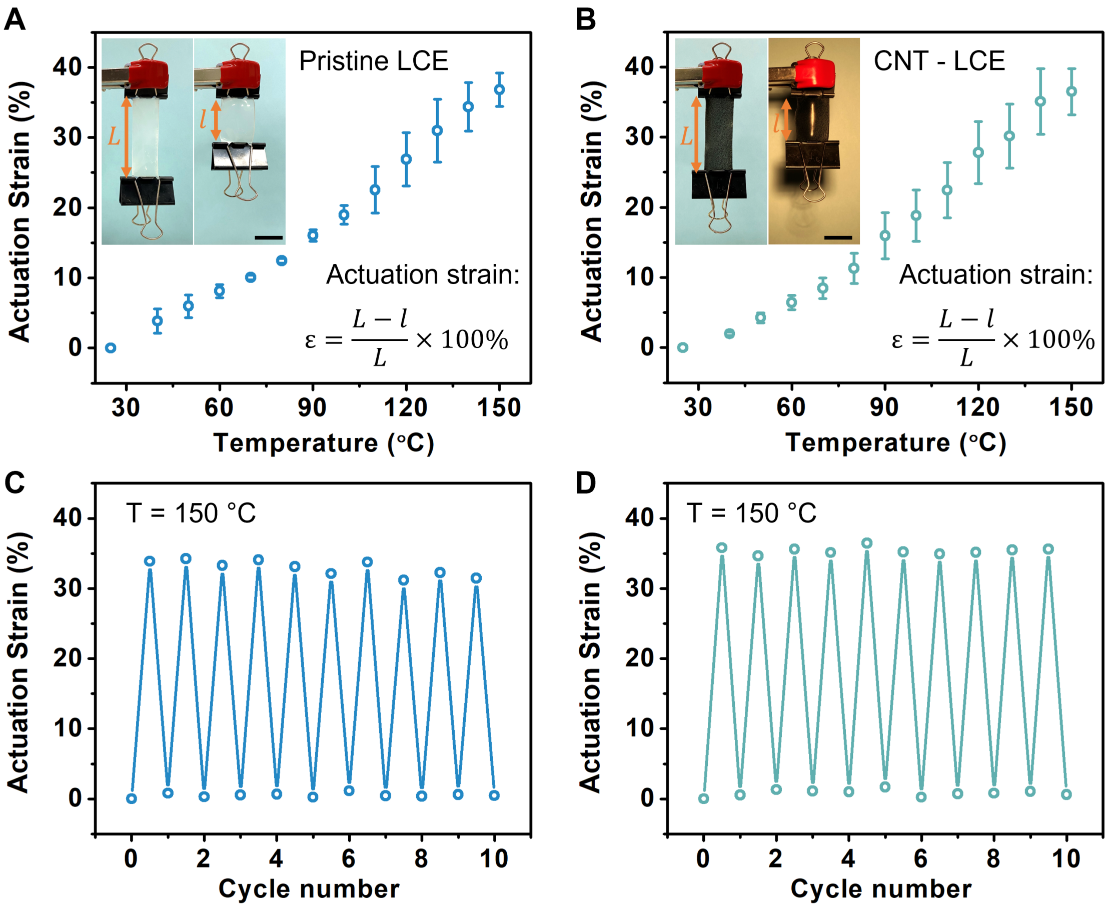

Figure S15: **The actuation strain and cycling tests of LCE (A, C) and CNT-LCE (B,D).** The actuation strain (ϵ) is defined as $\epsilon \equiv (L-l)/L \times 100\%$, where L is the length of the LCE at room temperature and l is the length of the LCE at high temperature. The actuation strain increases with the environmental temperature. Scale bar in **A** and **B**: 2 cm.

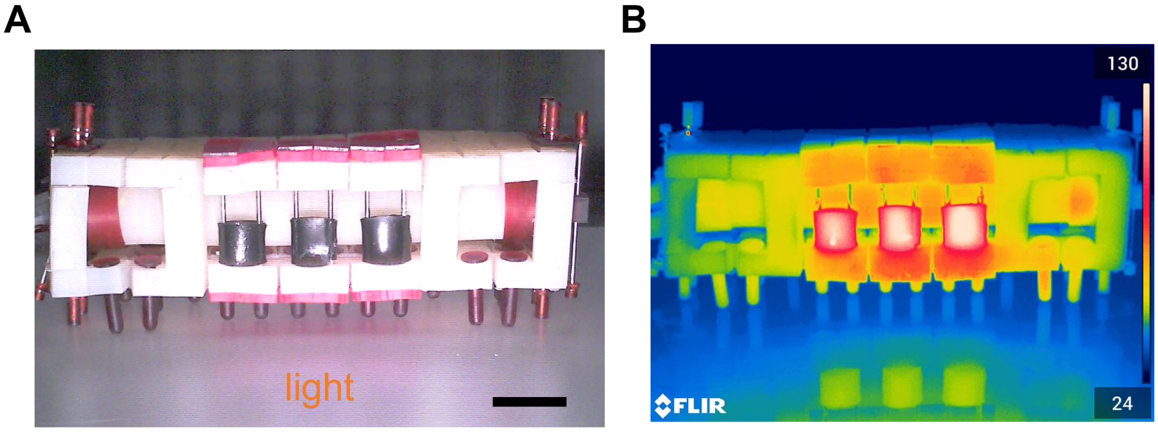

Figure S16: **The optical image (A) and infrared/thermal image (B) of the robot under light irradiation A.** The CNT-LCE composite strips have relatively higher temperature than the robot body, indicating the CNT-LCE composite strips can absorb light and convert to heat. Scale bar in **A**: 2 cm.

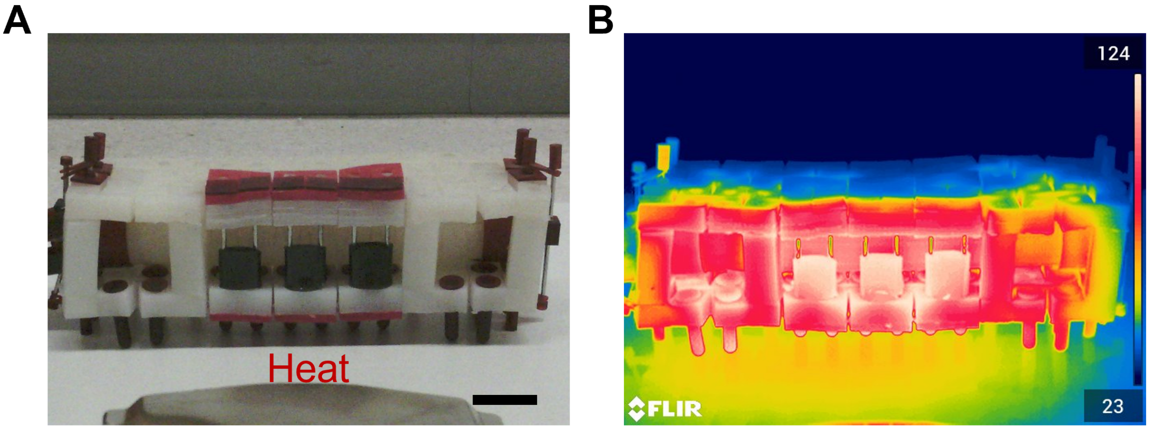

Figure S17: **The optical image (A) and infrared/thermal image (B) of the robot under the heat source A.** The temperatures of CNT-LCE composite strips and robot body are comparable. Scale bar in **A**: 2 cm.

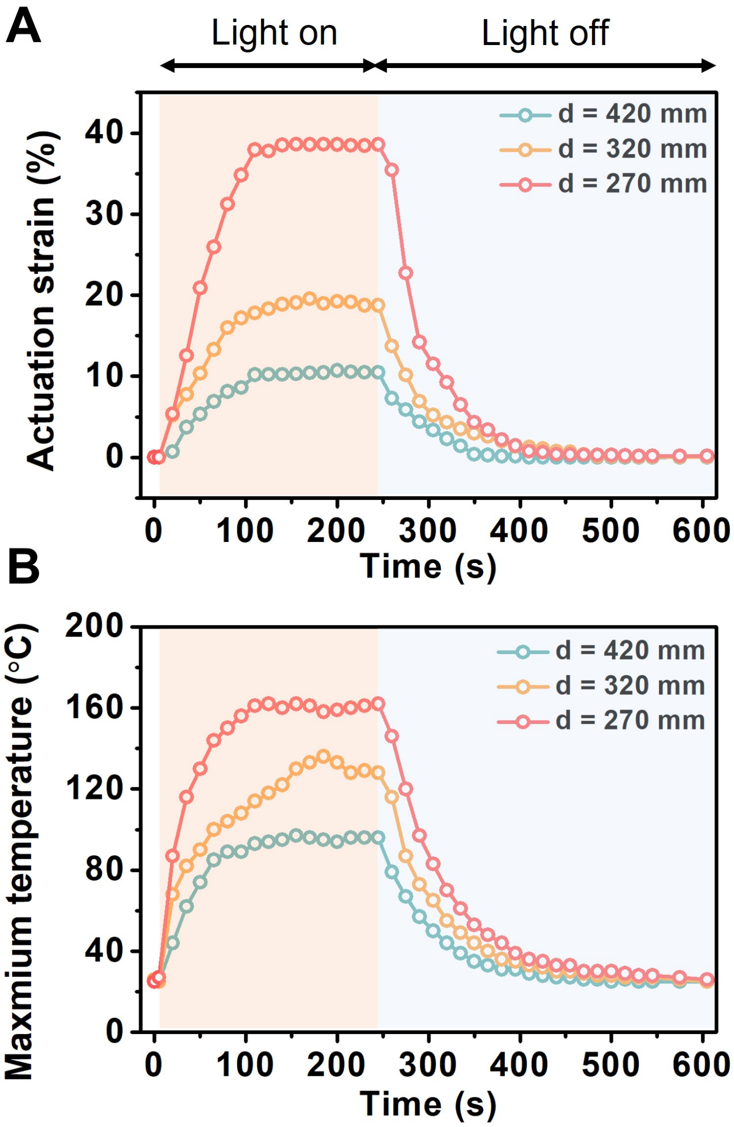

Figure S18: **The response of CNT-LCE under different lighting conditions. A.** Actuation strain as a function of time for the CNT-LCE film. In the experiment, the light is switched on for 240 s and then switched off (360 s). The light intensity can be varied by changing the distance between the light source and the sample (420 mm, 320 mm, and 270 mm). The actuation strain gradually increases when the light is switched on. After 100 s, the actuation strain reaches a constant value, corresponding to the steady state. When the light is switched off, the actuation strain drops to 0 within 160 s. **B.** The maximum surface temperature of the CNT-LCE film during the experiments.

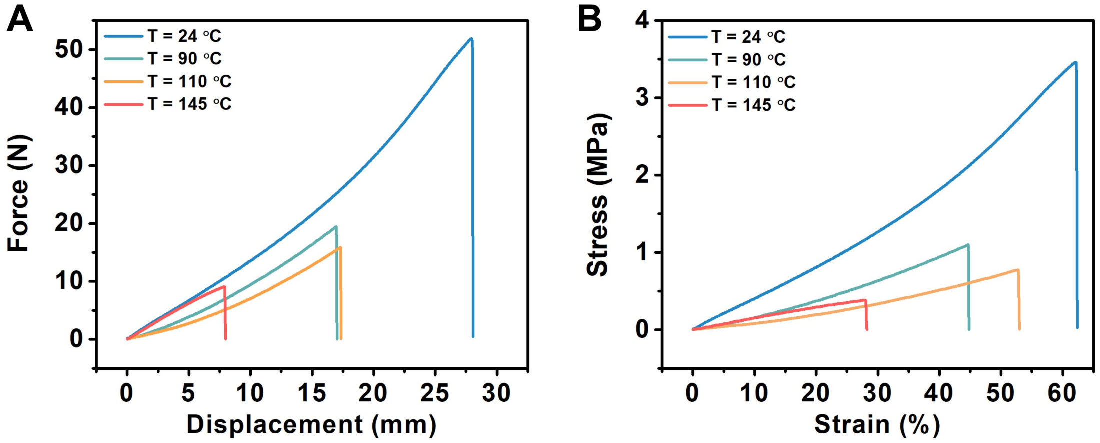

Figure S19: **The mechanical properties of the CNT-LCE film under different temperatures.** **A.** The force-displacement relationship of the CNT-LCE films (45 mm×15 mm ×1 mm) under different temperatures. The maximum force decreases from 50 N to 10 N when the temperature is elevated from 24 °C to 145 °C. **B.** The stress-strain relationship of the CNT-LCE under different temperatures. Both the strength and the stretchability of the CNT-LCE are decreased when the temperature is gradually increased.

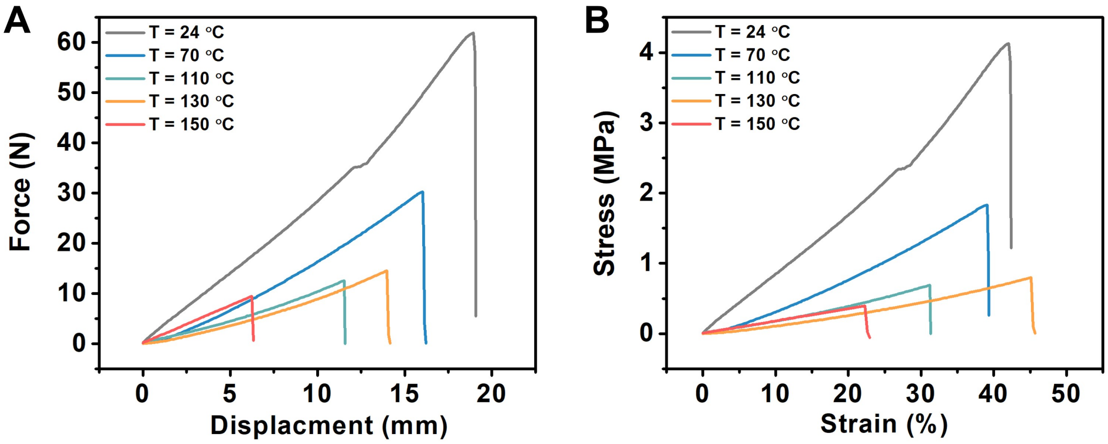

Figure S20: **The mechanical properties of the pristine LCE film under different temperatures. A.** The force-displacement relationship of the pristine LCE films (45 mm×15 mm ×1 mm) under different temperatures. The maximum force decreases from 60 N to 10 N when the temperature is elevated from 24 °C to 150 °C. **B.** The stress-strain relationship of the CNT-LCE under different temperatures. Both the strength and the stretchability of the CNT-LCE are decreased when the temperature is gradually increased.

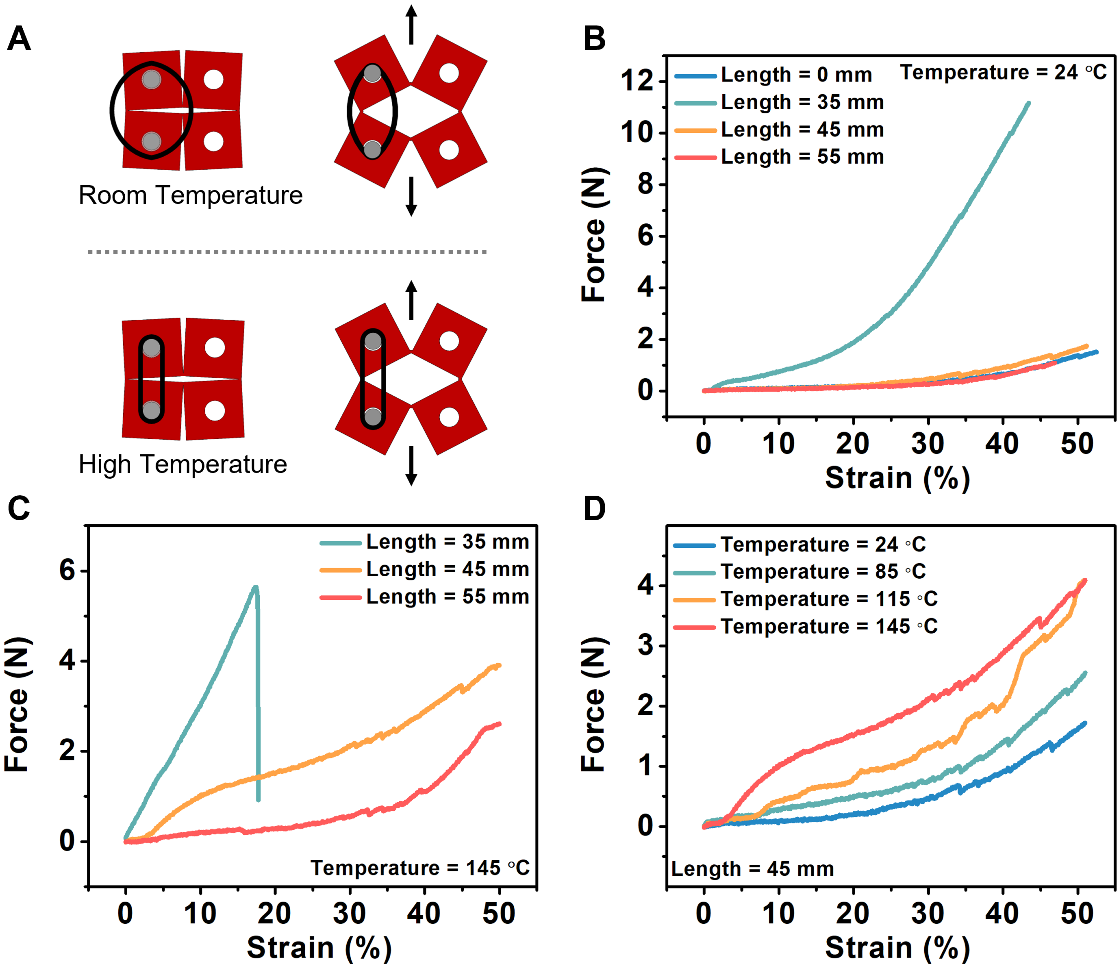

Figure S21: **Effect of the length of the CNT-LCE strip in the control modules.** **A.** Schematic of squares with CNT-LCE strips at different temperatures. **B.** A strip of length 35 mm is too short to allow free rotation of the kirigami at room temperature (24 °C). **C.** A strip of length 55 mm is too long to constrain the rotation of the squares, even at high temperature (145 °C). **D.** The length of the CNT-LCE strip is set to be 45 mm. At 25 °C, the pulling force gradually increases when the temperature is increased, which means the CNT-LCE strip constrains the rotation of the squares at high temperatures.

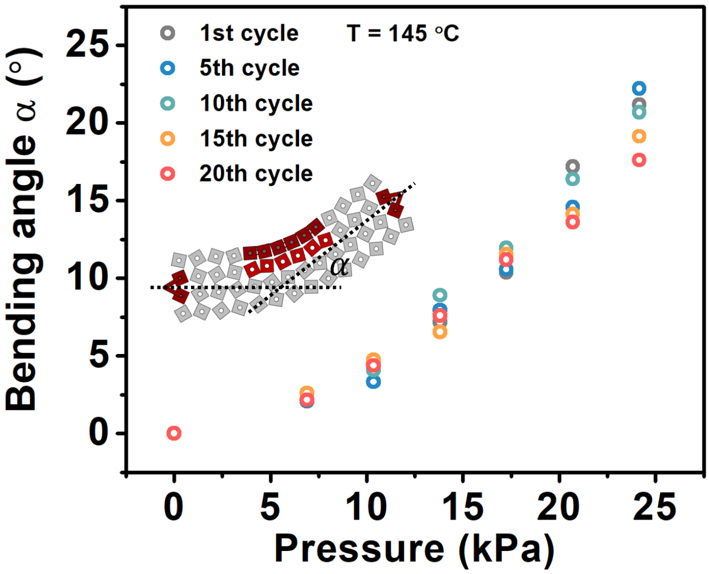

Figure S22: **The repeatability of the control module.** The experimental measurements of the bending angle α as a function of the applied pressure under twenty different inflation/deflation cycles at high temperature (145 °C).

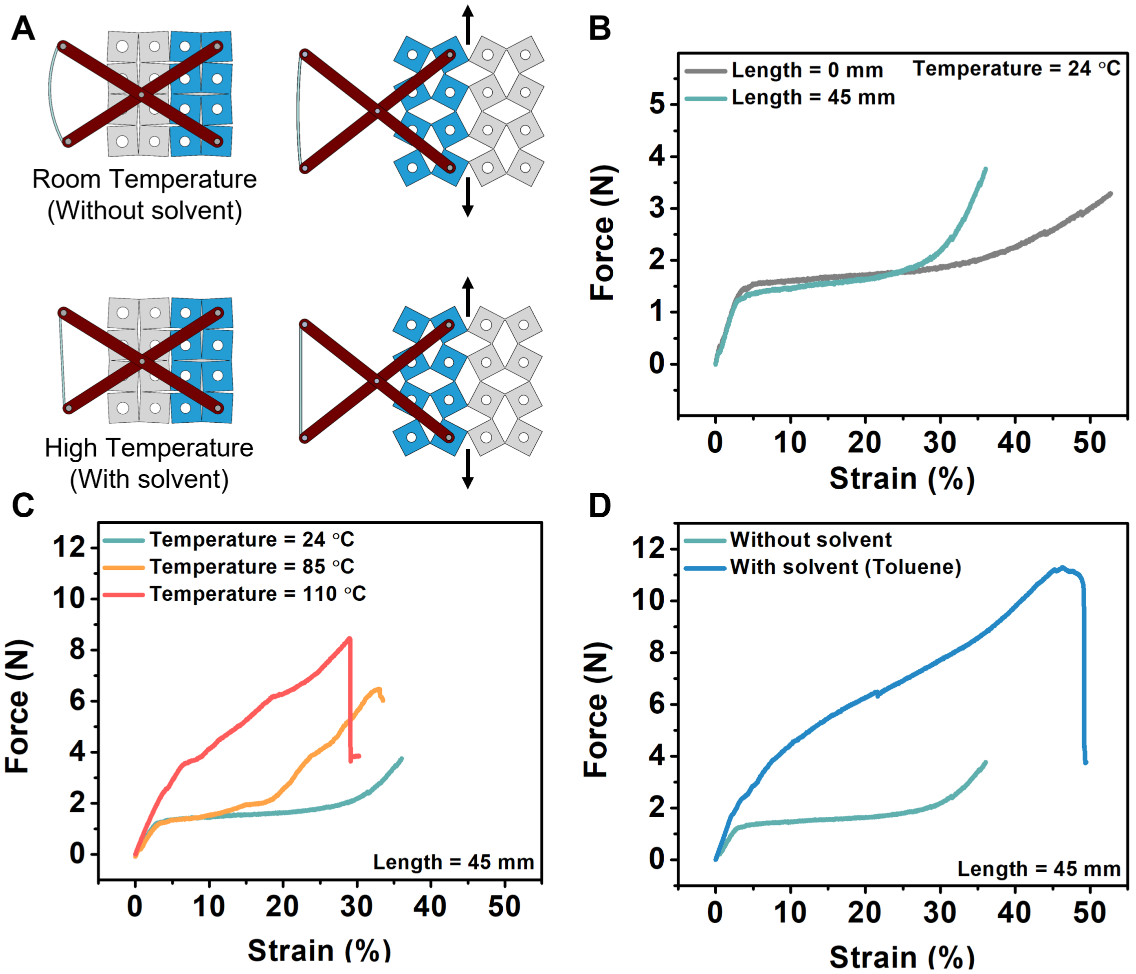

Figure S23: **Effect of the length of the LCE strip in the control modules. A.** Schematic of squares with LCE strips under different environments (temperatures or exposure of the solvent toluene). **B.** At room temperature, the pristine LCE cannot prevent the opening of the squares. **C.** When the temperature is increased, the pristine LCE strip contracts and generates tension. When the kirigami is stretched, the force at 25% strain gradually increases to above 1.8 N (the force at 25 percent strain under 24°C) when the temperature of the LCE is increased, which means that the pristine LCE can constrain the rotation of the squares. **D.** When the LCE strip is exposed to solvents, the LCE contracts due to a nematic-isotropic phase transition. The LCE can thereby generate force and constrain the rotation of the squares.

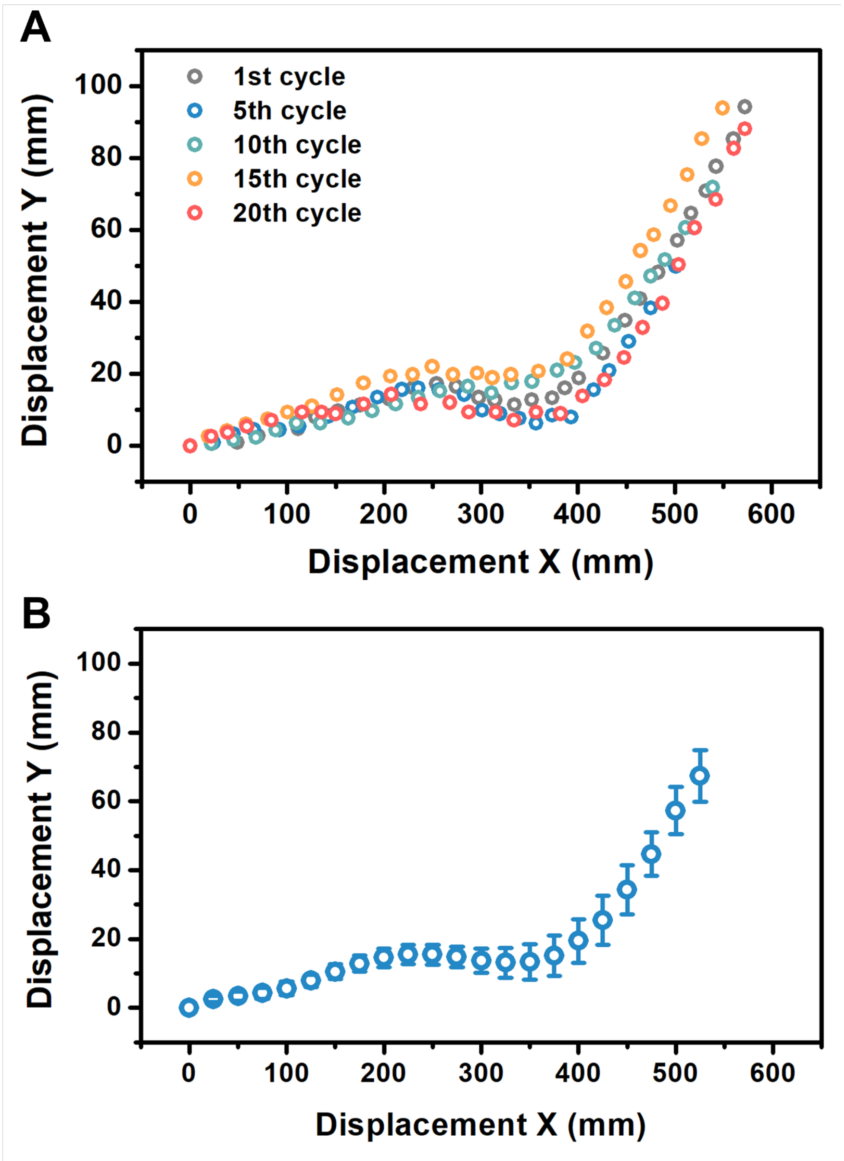

Figure S24: **The repeatability of the robot's trajectory.** The trajectory of the robot for 20 experiments with the same light conditions (The power of the light is 600 W and the distance between the light and robot is set to 320 mm).

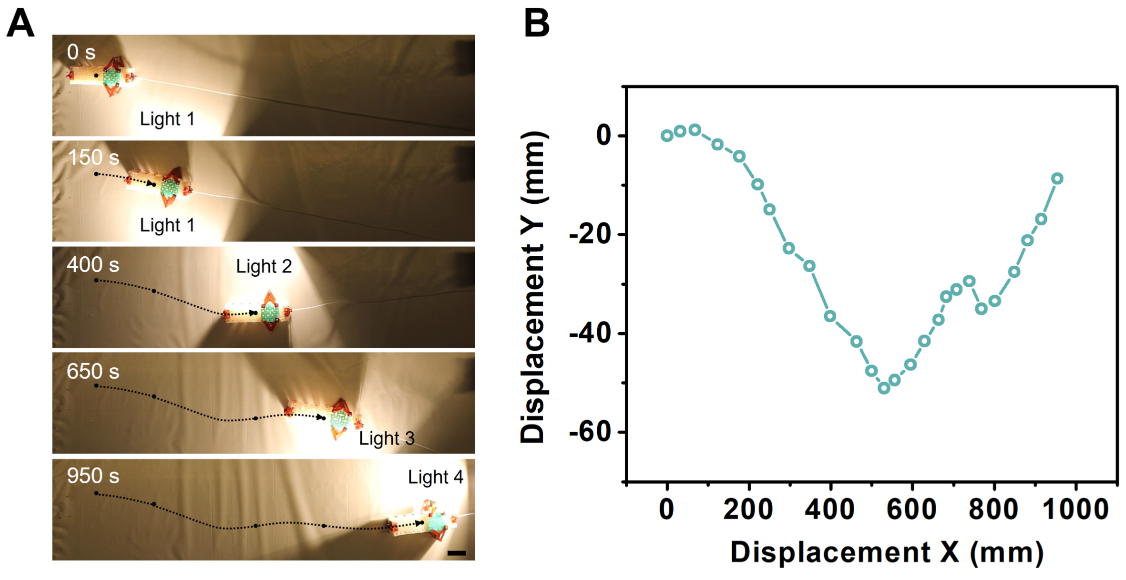

Figure S25: **The soft robot steers itself in a dynamic light environment.** The soft robot (integrated with control module 3) steers itself and moves toward the light as the light sources are sequentially switched on and off. Scale bar in **A**: 5 cm.

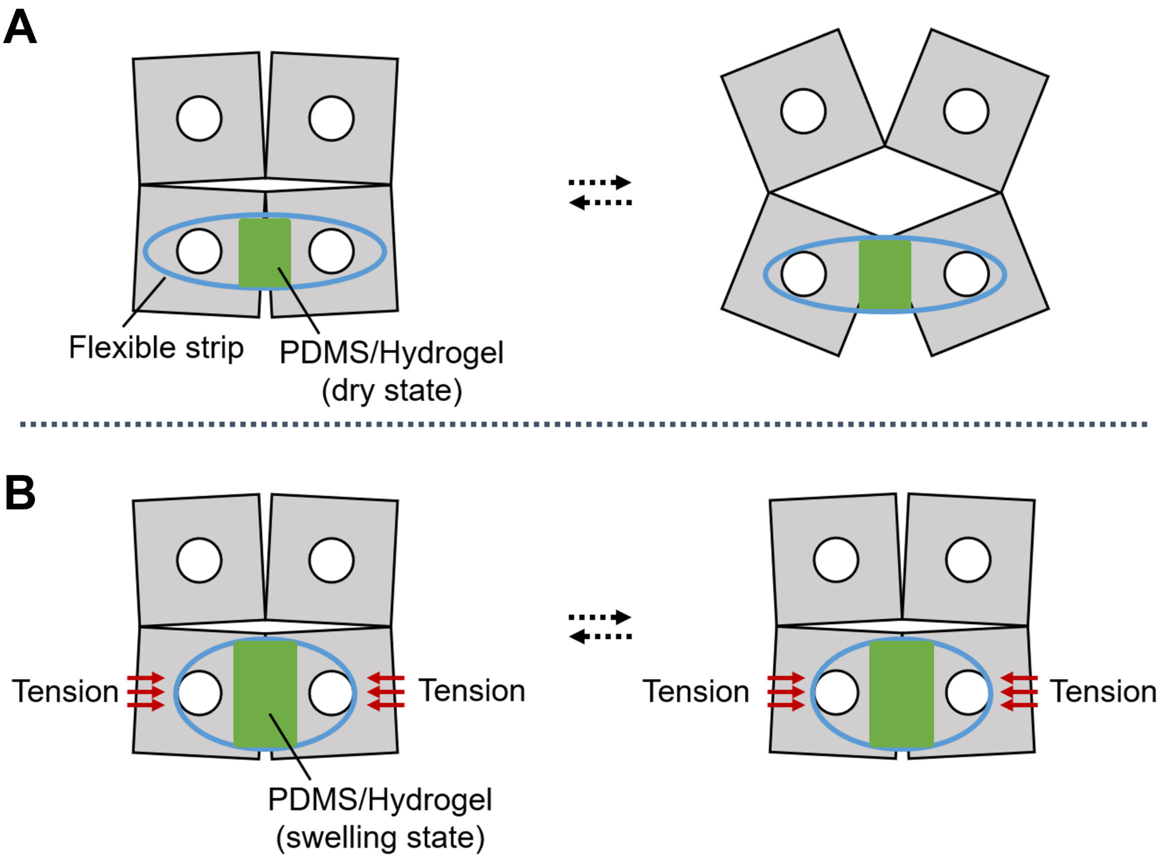

Figure S26: **Swelling mechanism of responsive materials (PDMS or hydrogels).** **A.** We attach the flexible strip with responsive materials (PDMS/hydrogel) onto the kirigami platform. The squares can freely open when there are no stimuli (solvents/water) present in the environment. **B.** If the control modules are subjected to solvents or water, the responsive materials swell, generating tension in the strip, preventing the square units from rotating and opening.

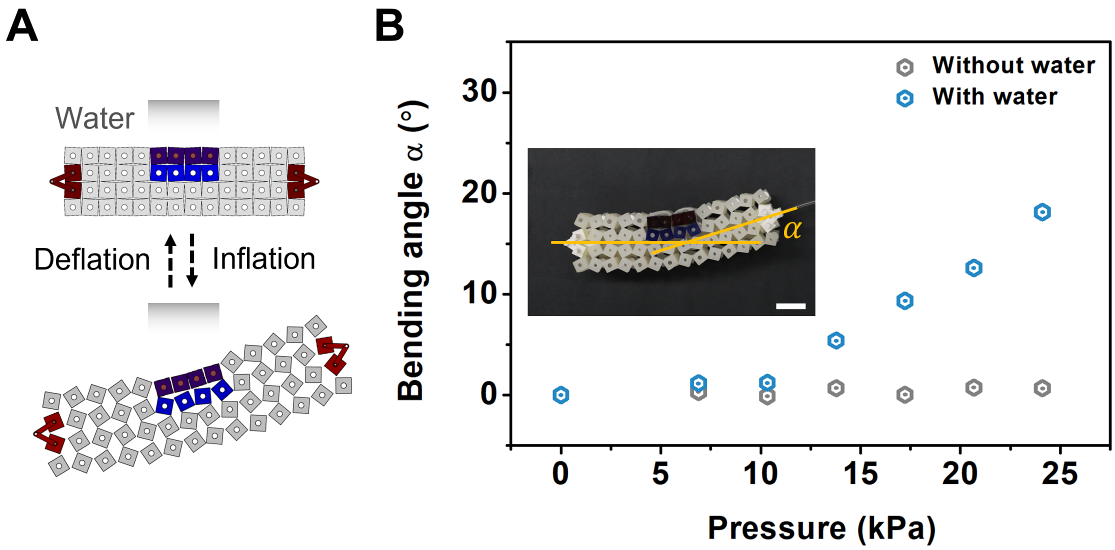

Figure S27: **The control module can sense and respond to water. A.** The control module (integrated with hydrogel) is submerged in water for 2 hours and then attached to the robot. The swollen hydrogel locally prevents the squares from opening when the pneumatic actuator is pressurized. Consequently, the robot bends in the same direction as the module. **B.** Bending angle α as a function of the applied pressure in different conditions (with water or without water). Scale bar in **B**: 2 cm.

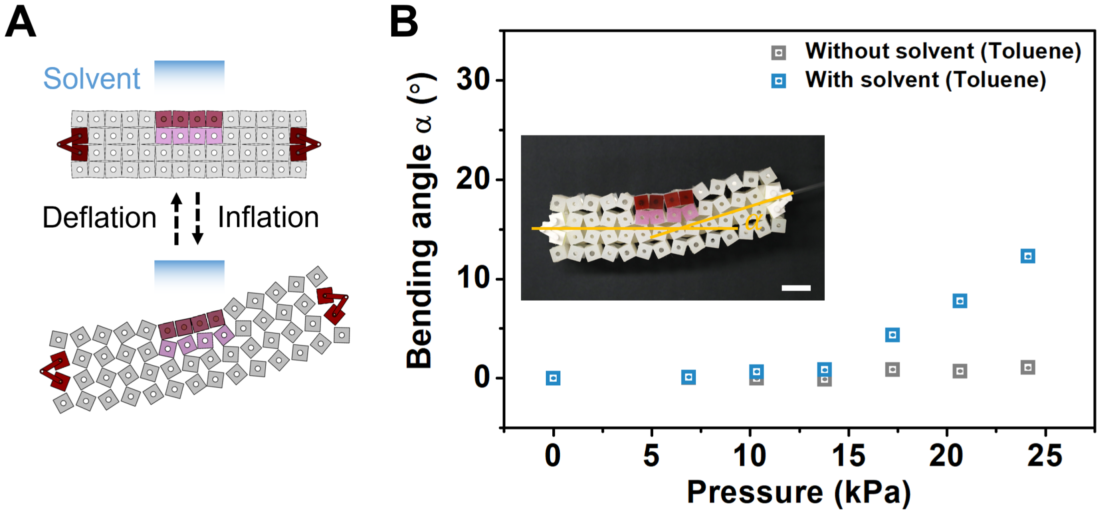

Figure S28: **The control module can sense and respond to toluene. A.** When the module is exposed to toluene, the silicone strip constrains the opening of the squares, causing the kirigami body to bend. In the experiment, we submerge the strip in toluene for 15 minutes and then reattach the strip to the robot. **B.** Experimental measurements of the bending angle α as a function of the applied pressure under different conditions (with toluene, without toluene). Scale bar in **B**: 2 cm.

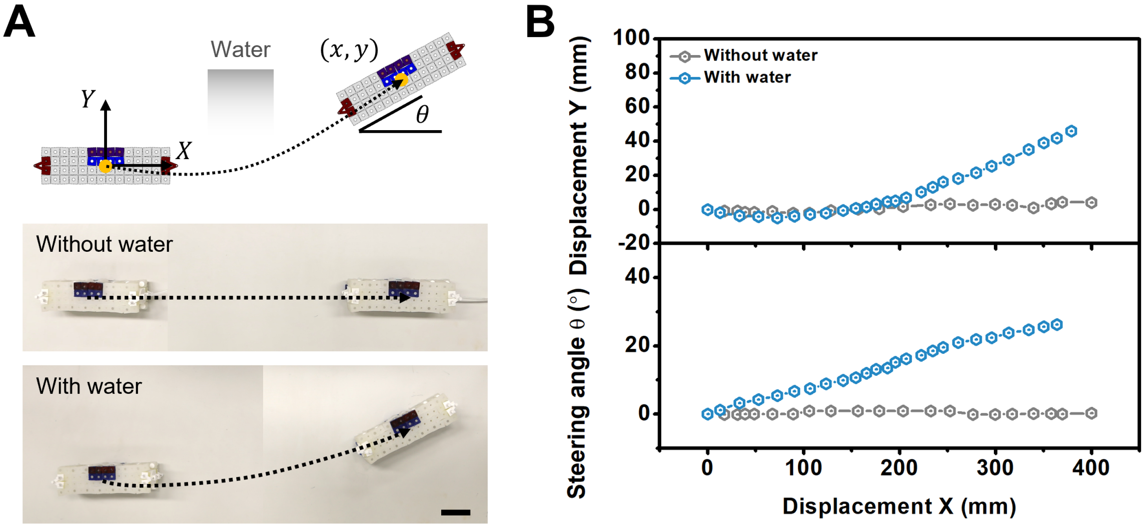

Figure S29: **Autonomous changes to trajectory in response to water. A.** The schematic and experimental images show that the robot can autonomously steer when exposed to water. When no water is present, the robot moves straight. **B.** The trajectory (displacement and steering angle) of the robot in different conditions (without water or with water in the environment). Scale bar: 5 cm.

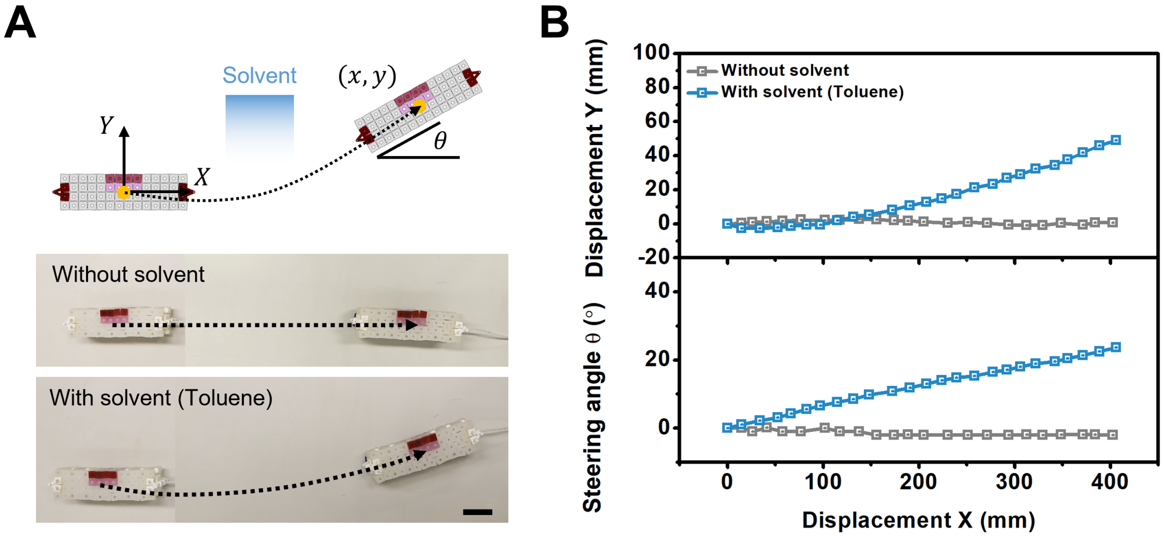

Figure S30: **Autonomous changes to trajectory in response to solvents (toluene).** **A.** The schematic and experimental images show the trajectory of the robot when it is exposed to toluene. **B.** The trajectory (displacement and steering angle) of the robot without and with toluene. Scale bar: 5 cm.

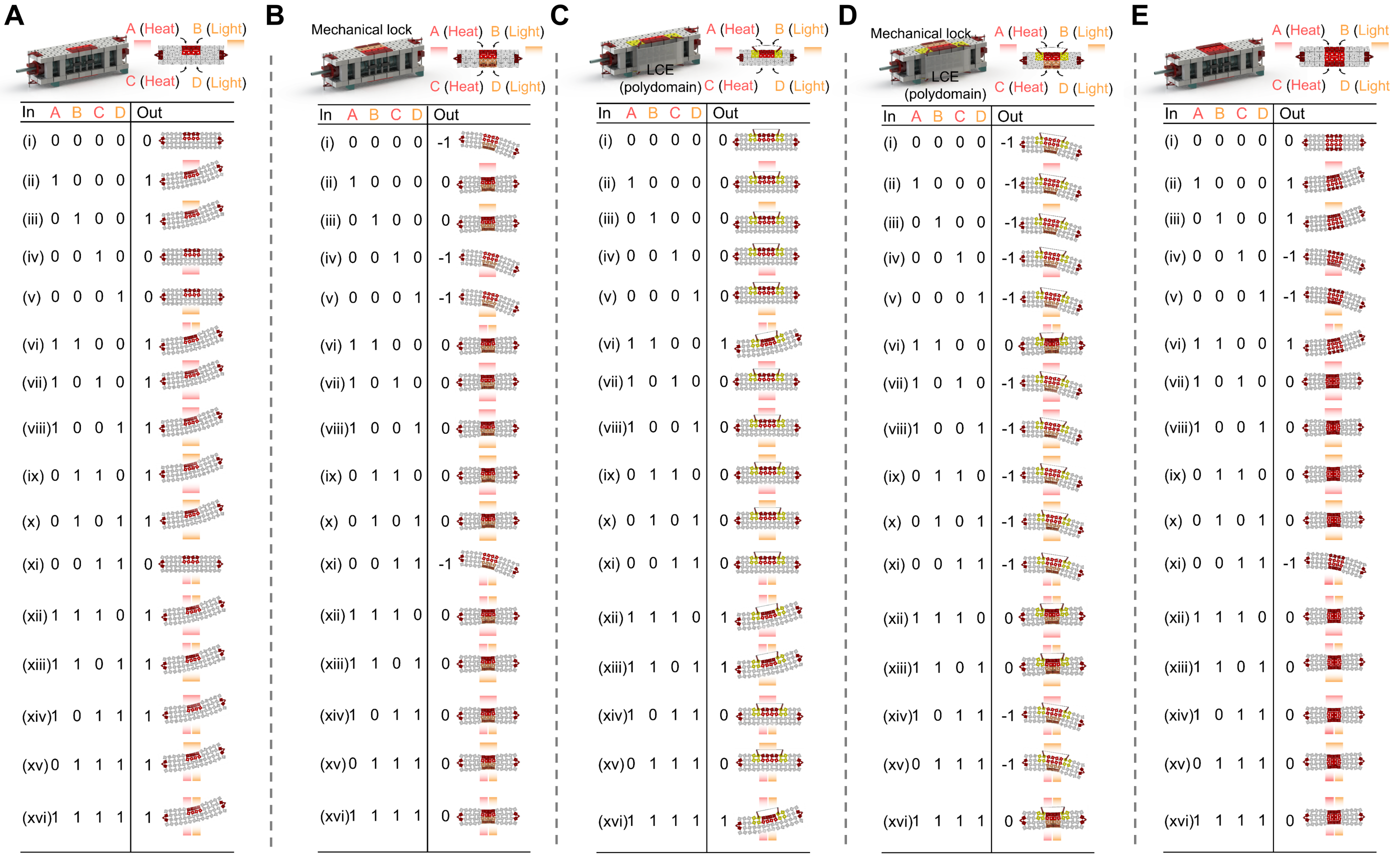

A

In	A	B	C	D	Out
(i)	0	0	0	0	0
(ii)	1	0	0	0	1
(iii)	0	1	0	0	1
(iv)	0	0	1	0	0
(v)	0	0	0	1	0
(vi)	1	1	0	0	1
(vii)	1	0	1	0	1
(viii)	1	0	0	1	1
(ix)	0	1	1	0	1
(x)	0	1	0	1	1
(xi)	0	0	1	1	0
(xii)	1	1	1	0	1
(xiii)	1	1	0	1	1
(xiv)	1	0	1	1	1
(xv)	0	1	1	1	1
(xvi)	1	1	1	1	1

B

In	A	B	C	D	Out
(i)	0	0	0	0	-1
(ii)	1	0	0	0	0
(iii)	0	1	0	0	0
(iv)	0	0	1	0	-1
(v)	0	0	0	1	-1
(vi)	1	1	0	0	0
(vii)	1	0	1	0	0
(viii)	1	0	0	1	0
(ix)	0	1	1	0	0
(x)	0	1	0	1	0
(xi)	0	0	1	1	-1
(xii)	1	1	1	0	0
(xiii)	1	1	0	1	0
(xiv)	1	0	1	1	0
(xv)	0	1	1	1	0
(xvi)	1	1	1	1	0

C

In	A	B	C	D	Out
(i)	0	0	0	0	0
(ii)	1	0	0	0	0
(iii)	0	1	0	0	0
(iv)	0	0	1	0	0
(v)	0	0	0	1	0
(vi)	1	1	0	0	1
(vii)	1	0	1	0	0
(viii)	1	0	0	1	0
(ix)	0	1	1	0	0
(x)	0	1	0	1	0
(xi)	0	0	1	1	0
(xii)	1	1	1	0	1
(xiii)	1	1	0	1	1
(xiv)	1	0	1	1	0
(xv)	0	1	1	1	0
(xvi)	1	1	1	1	1

D

In	A	B	C	D	Out
(i)	0	0	0	0	-1
(ii)	1	0	0	0	-1
(iii)	0	1	0	0	-1
(iv)	0	0	1	0	-1
(v)	0	0	0	1	-1
(vi)	1	1	0	0	0
(vii)	1	0	1	0	-1
(viii)	1	0	0	1	-1
(ix)	0	1	1	0	-1
(x)	0	1	0	1	-1
(xi)	0	0	1	1	-1
(xii)	1	1	1	0	0
(xiii)	1	1	0	1	0
(xiv)	1	0	1	1	-1
(xv)	0	1	1	1	-1
(xvi)	1	1	1	1	0

E

In	A	B	C	D	Out
(i)	0	0	0	0	0
(ii)	1	0	0	0	1
(iii)	0	1	0	0	1
(iv)	0	0	1	0	-1
(v)	0	0	0	1	-1
(vi)	1	1	0	0	1
(vii)	1	0	1	0	0
(viii)	1	0	0	1	0
(ix)	0	1	1	0	0
(x)	0	1	0	1	0
(xi)	0	0	1	1	-1
(xii)	1	1	1	0	0
(xiii)	1	1	0	1	0
(xiv)	1	0	1	1	0
(xv)	0	1	1	1	0
(xvi)	1	1	1	1	0

Figure S31: **"Truth tables" that relate inputs (i.e., the stimuli in the environment) to outputs (i.e., trajectory) for several different control modules. The distance between the robot and the energy source is 200 mm to prevent overheating from occurring too rapidly.**

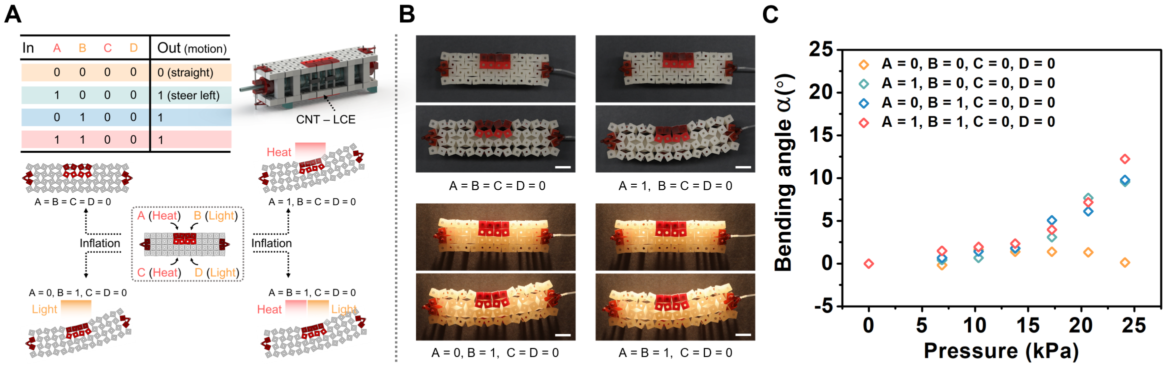

Figure S32: **"OR" response of the robot. A.** A single CNT-LCE module (Fig. 3C) acts like a logical "OR". **B.** The experimental images of the robot under different light and heat conditions. When the robot is subjected to light or heat, the control module is activated, causing the robot to bend to the left. **C.** Measurements of bending angle α as a function of the applied pressure under different light and heat conditions. Scale bar in **B**: 2 cm.

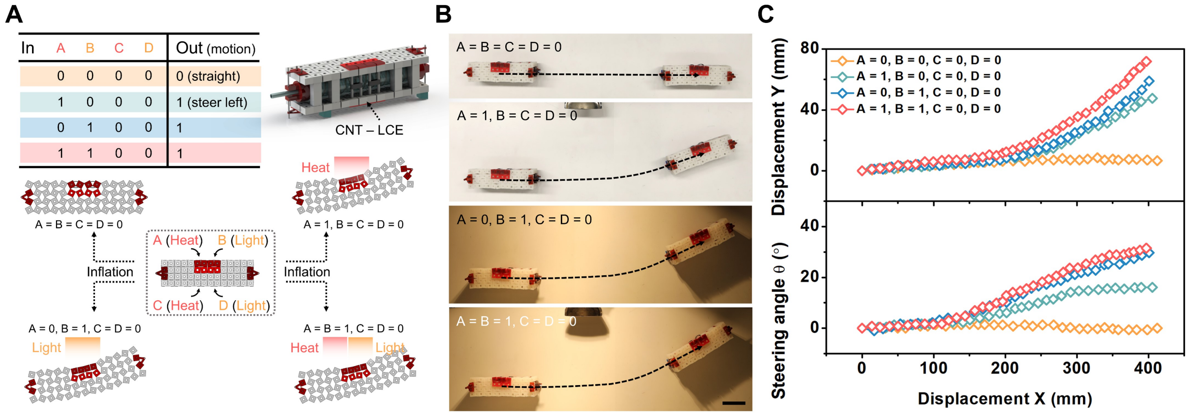

In	A	B	C	D	Out (motion)
	0	0	0	0	0 (straight)
	1	0	0	0	1 (steer left)
	0	1	0	0	1
	1	1	0	0	1

Figure S33: **The trajectory caused by an "OR" module of the previous figure.** **A.** The truth table of the "OR" response. **B-C.** Experimental images and trajectories, respectively, of the robot with different heat or light inputs. Scale bar in **B**: 5 cm.

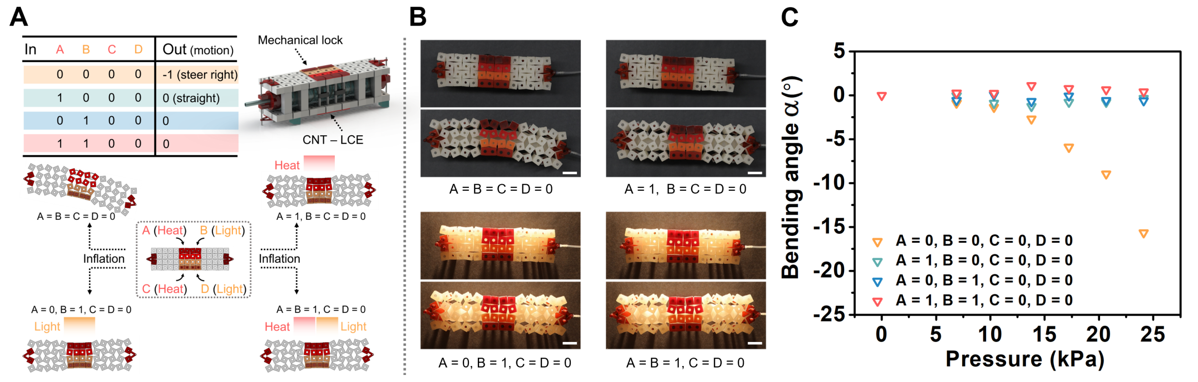

In	A	B	C	D	Out (motion)
	0	0	0	0	-1 (steer right)
	1	0	0	0	0 (straight)
	0	1	0	0	0
	1	1	0	0	0

Figure S34: **"NOR" response of the robot.** **A.** For the "NOR" response, we attach a "mechanical lock" module and a CNT-LCE module (i.e., Fig. 3C) to the body of the robot. **B.** The experimental images of the robot under different light and heat conditions. With no stimuli present (A = B = C = D = 0), the mechanical lock causes the robot to bend to the right. When the CNT-LCE control module is subjected to heat or light from the left, the activation of the module cancels the effect of the mechanical lock, causing the robot to move straight ahead. **C.** Measurements of bending angle α as a function of the applied pressure under different light and heat conditions. Scale bar in **B**: 2 cm.

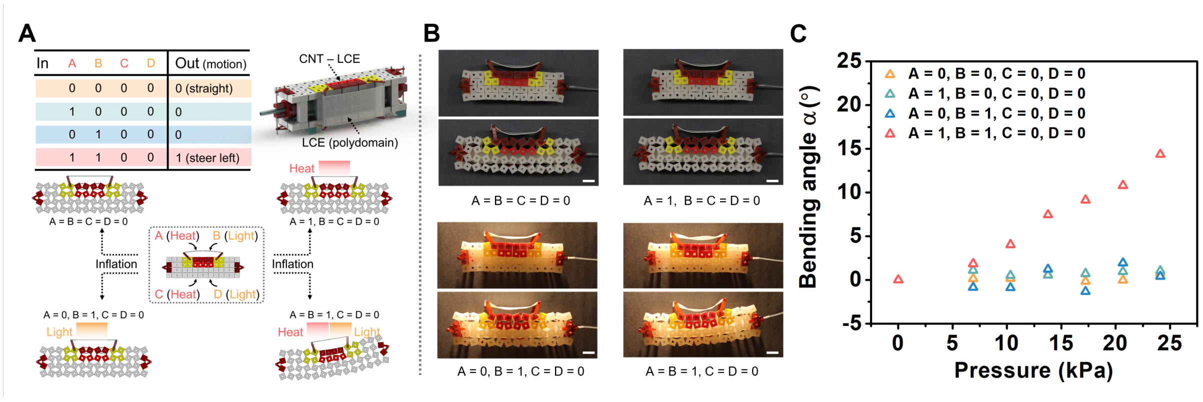

Figure S35: **"AND" response of the robot. A.** For the "AND" response, we attach a mask control module to the exterior of a CNT-LCE module (Fig. 3C). **B.** The experimental images of the robot under different light and heat conditions. When the robot is exposed to only heat or light from the left side, (A = 1, B = C = D = 0 or A = 0, B = 1, C = D = 0), the CNT-LCE cannot be actuated because the mask blocks the stimulus. Therefore the robot moves straight ahead. If the robot is exposed to both heat and light (A = B = 1, C = D = 0), the mask becomes transparent, allowing light to pass through it to actuate the inner CNT-LCE module. As a result, the robot bends to the left. **C.** Measurement of the bending angle α as a function of the applied pressure under different light and heat conditions. Scale bar in **B**: 2 cm.

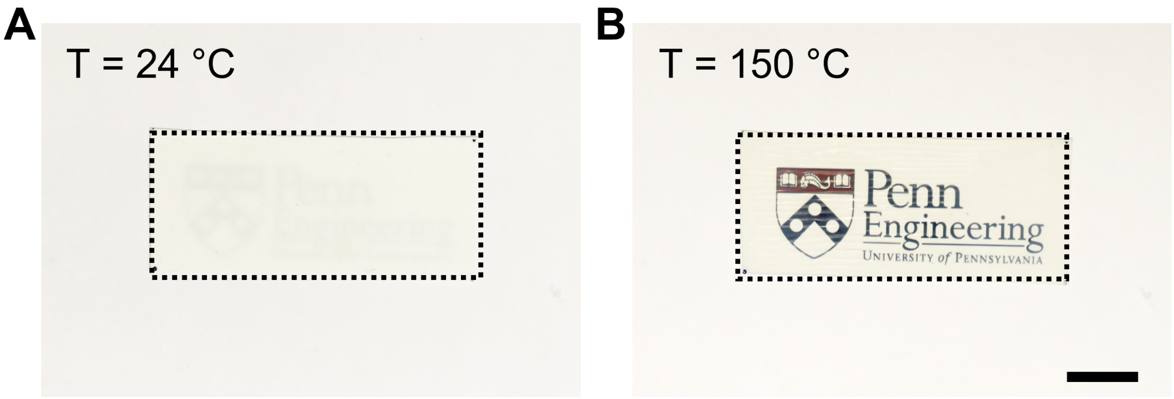

Figure S36: **The polydomain LCE changes its transparency when the temperature is increased A.** At room temperature, the polydomain LCE is opaque. **B.** At high temperature, the LCE is transparent due to a nematic-isotropic phase transition. Scale bar in **B**: 2 cm.

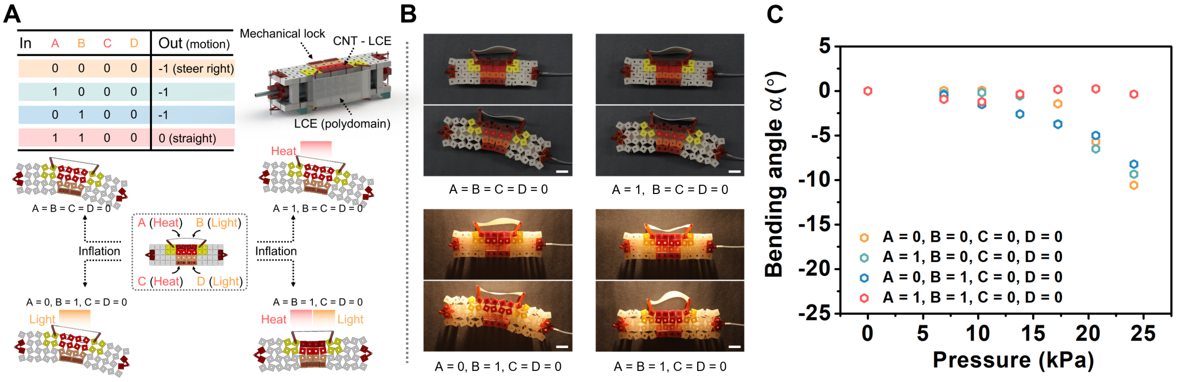

In	A	B	C	D	Out (motion)
	0	0	0	0	-1 (steer right)
	1	0	0	0	-1
	0	1	0	0	-1
	1	1	0	0	0 (straight)

Figure S37: **“NAND” response of the robot. A.** For the “NAND” response, we use a “mechanical lock” module, “mask” module, and CNT-LCE module. **B.** The robot bends to the right when subjected to only heat or light from the left side (A = 1, B = C = D = 0 or A = 0, B = 1, C = D = 0). However, if the robot is exposed to both heat and light, the mechanical constraints on the two sides cancel one another, causing the robot to move straight ahead. **C.** Measurement of the bending angle α as a function of the applied pressure under different light and heat conditions. Scale bar in **B**: 2 cm.

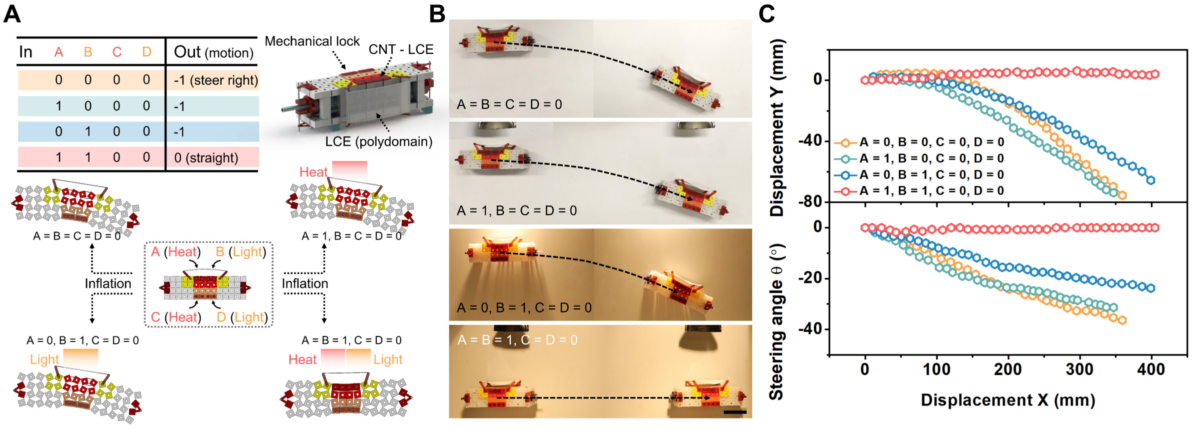

Figure S38: **The trajectories caused by a “NAND” response. A.** The truth table of the “NAND” response. **B-C.** Experimental images and trajectories, respectively, of the robot with different heat or light inputs. Scale bar in **B**: 2 cm.

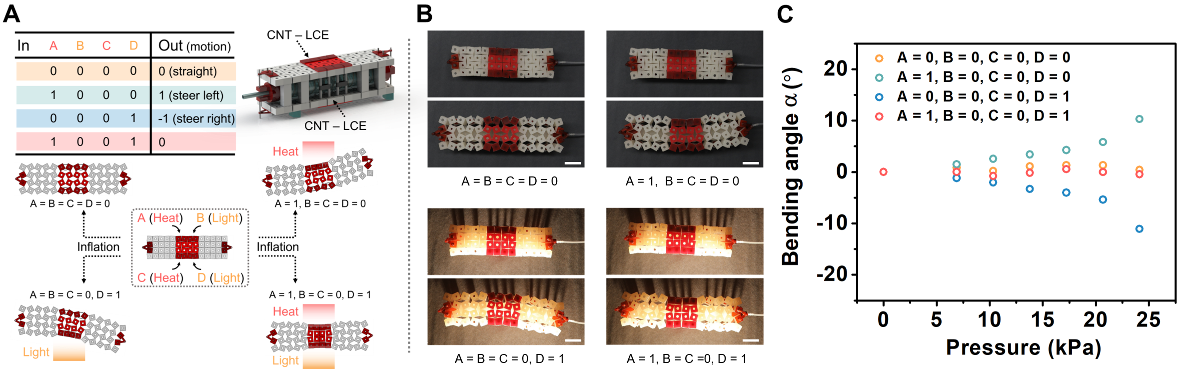

In	A	B	C	D	Out (motion)
	0	0	0	0	0 (straight)
	1	0	0	0	1 (steer left)
	0	0	0	1	-1 (steer right)
	1	0	0	1	0

Figure S39: **"XOR" response of the robot. A.** In this case, two identical control modules are distributed symmetrically along the two sides of the robot body. **B.** When one side of the control module is subjected to light or heat, the body of the robot bends toward the stimulus. If the control modules on both sides are active, their effects cancel, causing the robot to move straight ahead. **C.** Measurement of the bending angle α as a function of the applied pressure under different light and heat conditions. Scale bar in **B**: 2 cm.

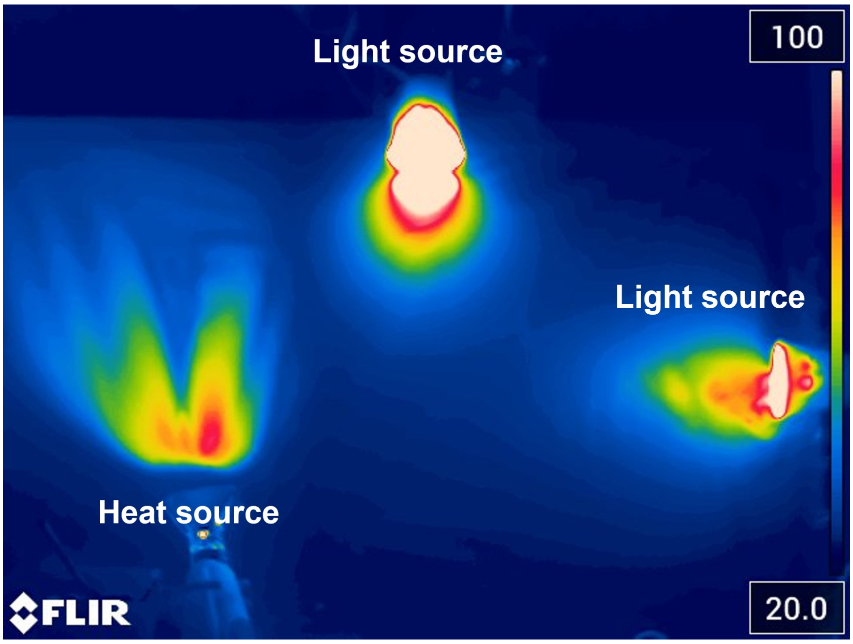

Figure S40: **An infrared / thermal image of the environment with multiple external stimuli.**

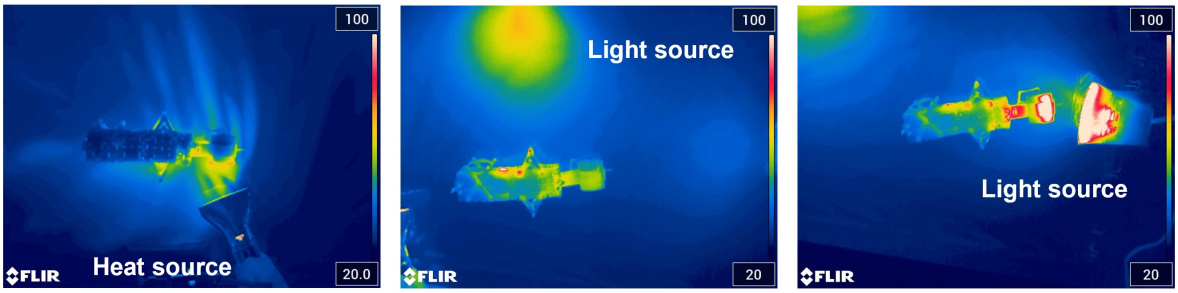

Figure S41: **Additional thermal images of the electronics-free soft robot in different environments.**

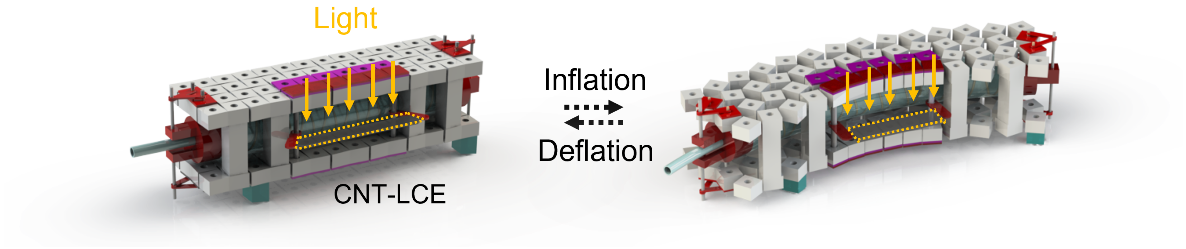

Figure S42: **The robot can sense and respond to light from the top.**

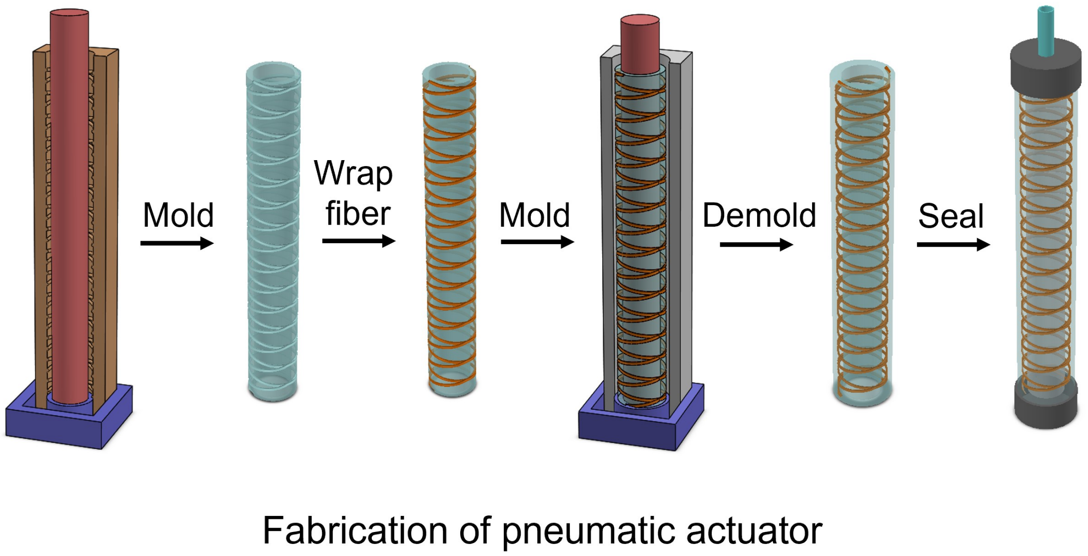

Figure S43: **Fabrication of the pneumatic actuator.** The pneumatic actuator is fabricated following a conventional molding-casting process. The silicone precursor (Ecoflex 30) is poured into the 3D printed mold and cured. Then, a kevlar fiber is wrapped on the surface of the cured silicone tube. After that, we encapsulate the kevlar fiber by pouring another layer of the silicone precursor. Two caps are finally glued to the tube and we insert an air tube at one end.

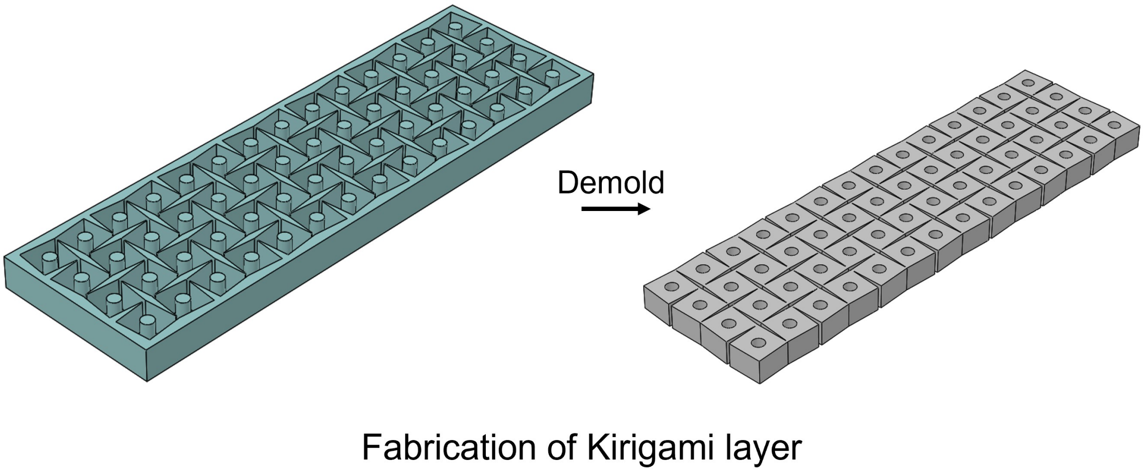

Figure S44: **Fabrication of the rotating squares kirigami platform.** The rotating squares kirigami platform is fabricated following a conventional molding-casting process. The silicone precursor (Dragonskin 10) is poured into the 3D-printed mold and cured.

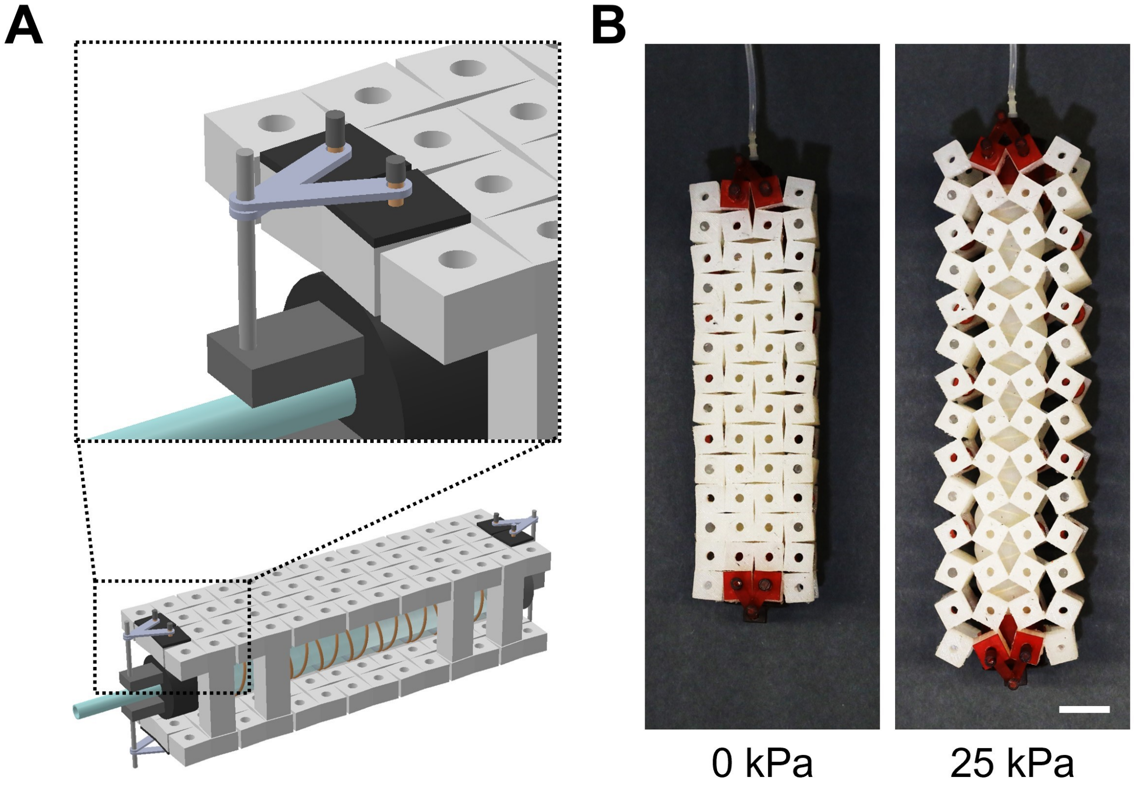

Figure S45: **Connecting the kirigami body and pneumatic actuator.** **A.** Schematic shows how the actuator and kirigami body are connected to each other. **B.** All the squares can be freely opened when pressure is applied to the pneumatic actuator. The actuator does not buckle when the applied pressure is 25 kPa. Scale bar in **B.** 2 cm.

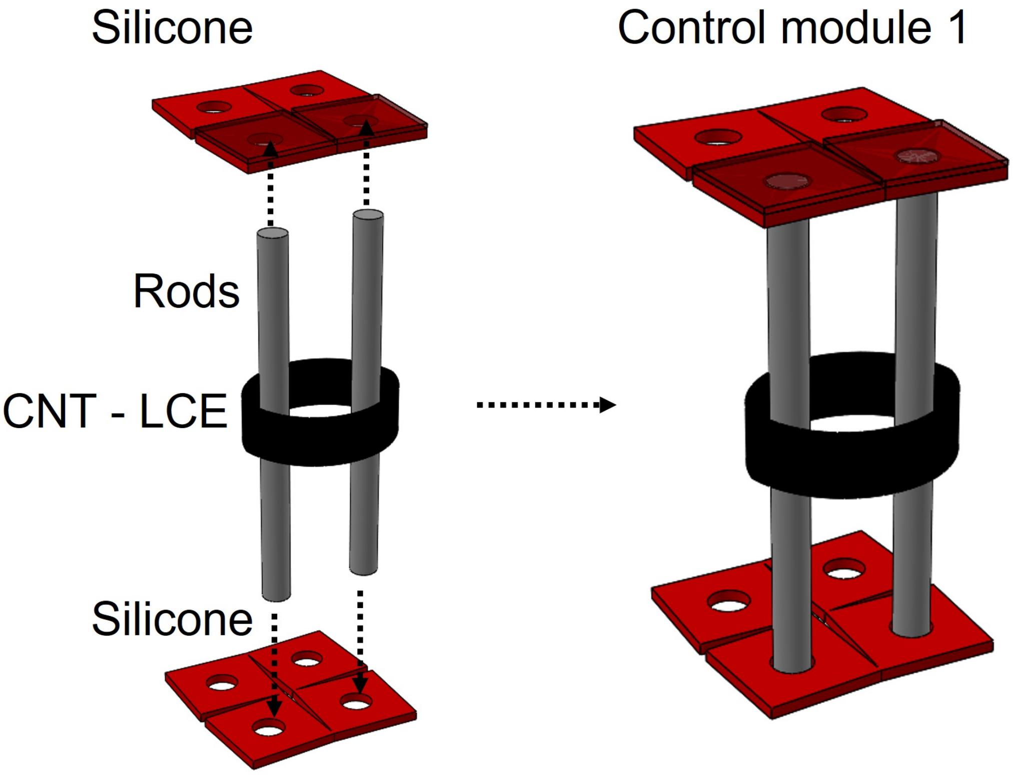

Figure S46: **The detailed structure of control module 1.** This control module consists of two layers of the silicone kirigami (red), two rigid rods, and a CNT-LCE strip.

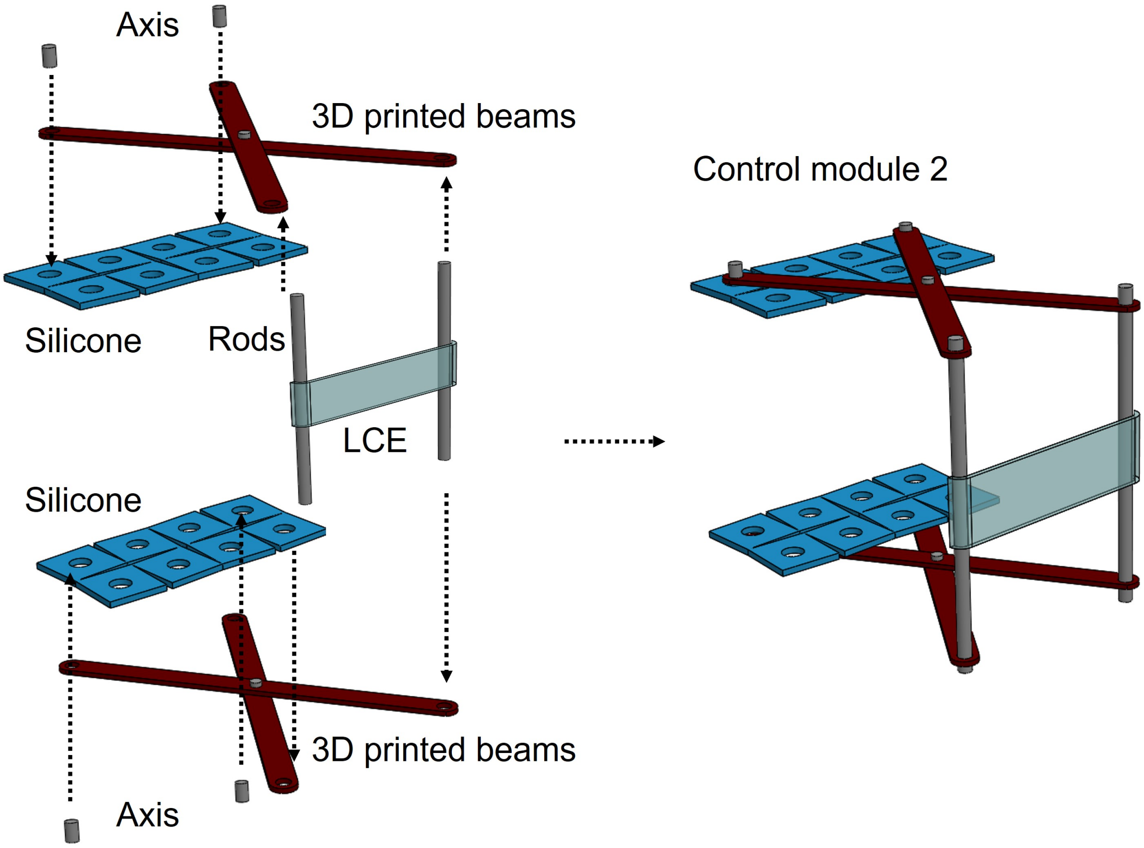

Figure S47: **The detailed structure of control module 2.** This control module consists of two layers of the silicone kirigami (blue), four 3D-printed beams, two rigid rods, and a LCE strip.

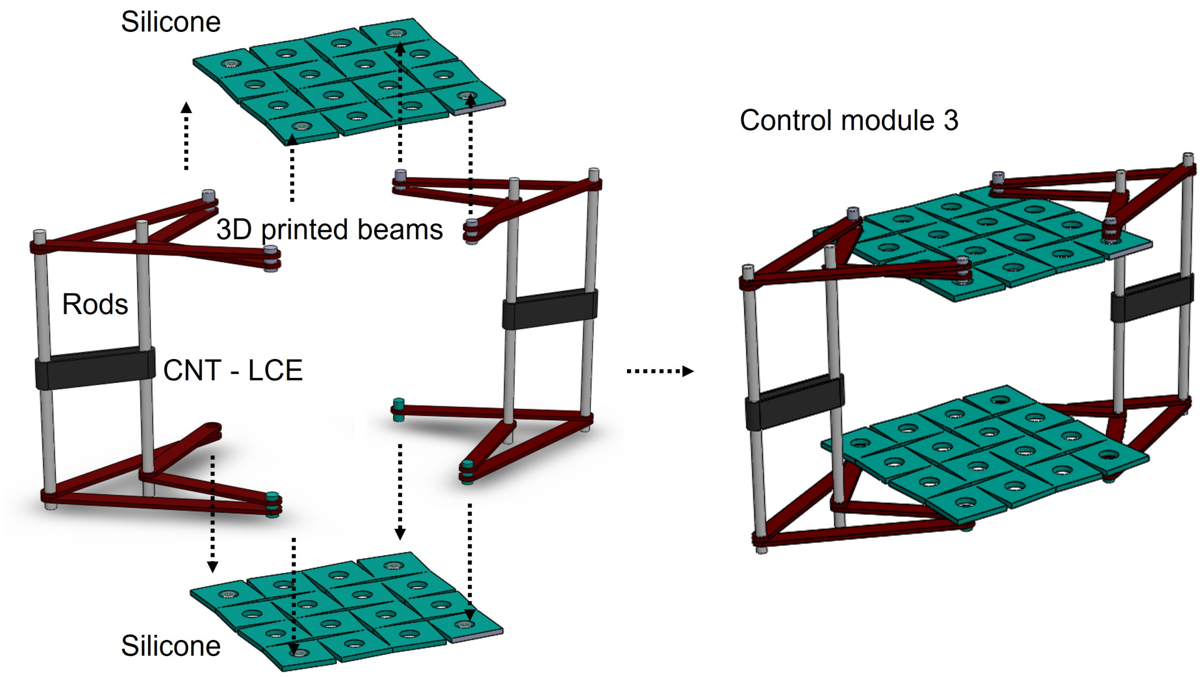

Figure S48: **The detailed structure of control module 3.** This control module consists of two layers of the silicone kirigami (green), sixteen 3D-printed beams, four rigid rods, and two CNT-LCE strips.

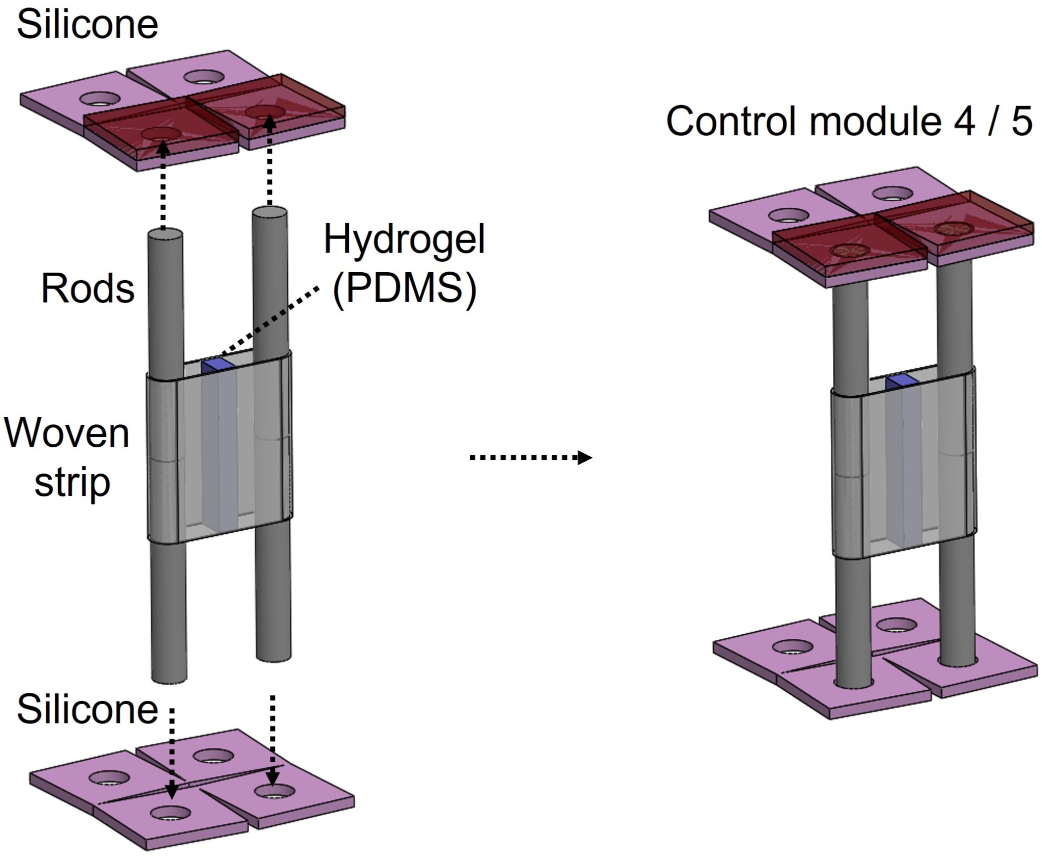

Figure S49: **The detailed structure of control modules 4 and 5.** This control module consists of two layers of the silicone kirigami (pink), two rigid rods, and a woven strip integrated with hydrogel or PDMS.

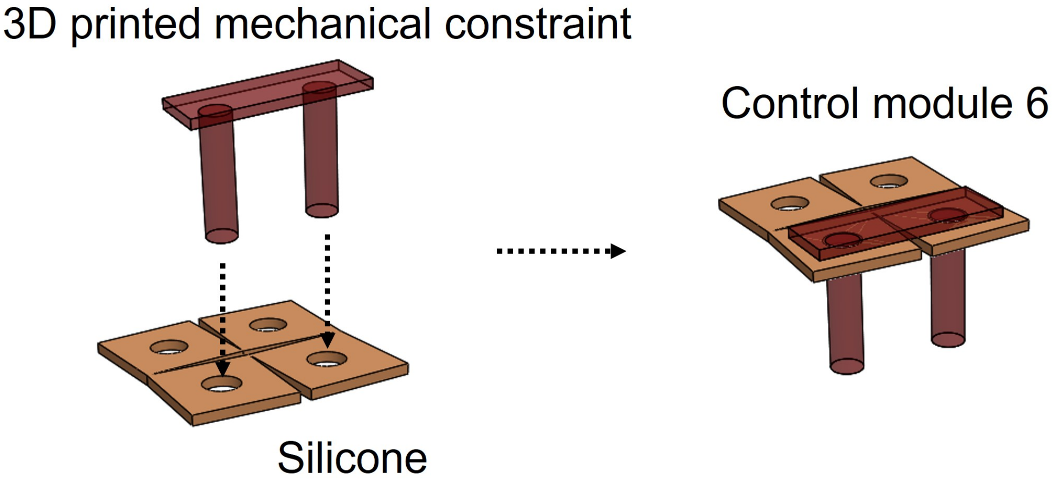

Figure S50: **The detailed structure of control module 6.** This control module consists of a layer of the silicone kirigami (orange), and a 3D-printed mechanical constraint.

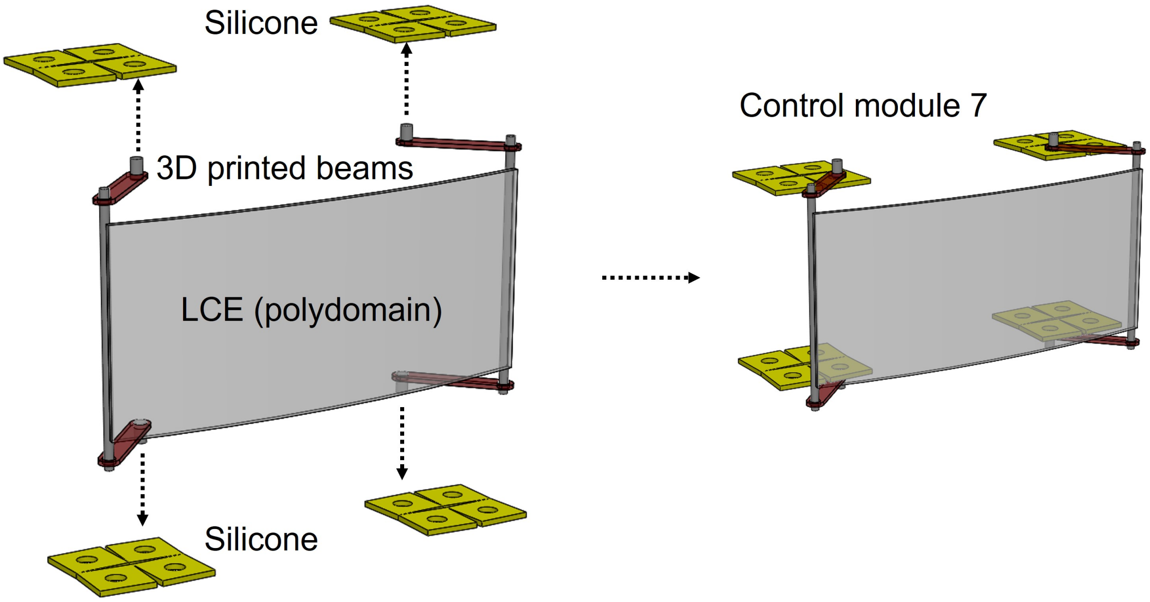

Figure S51: **The detailed structure of control module 7.** This control module consists of four layers of the silicone kirigami (yellow), and four 3D-printed beams, two rigid rods, and a polydomain LCE.

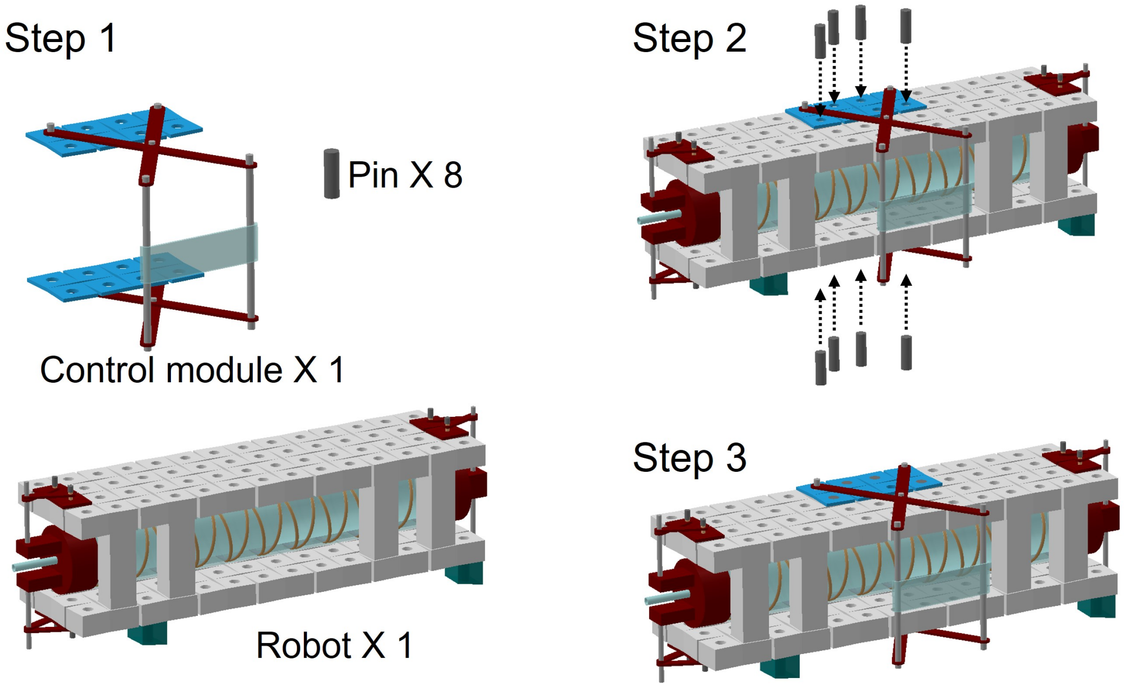

Figure S52: **Integration of the control modules.** The silicone kirigami of the control module (blue) is attached to the kirigami layers (gray) of the soft robot. Eight pins are inserted into the holes of the kirigami to connect the control module and robot.

Movie S1. Modularity of multiple types of control units.

Movie S2. Soft robot (without control modules) moves straight.

Movie S3. Soft robot steers trajectory closer to heat or light.

Movie S4. Soft robot steers trajectory away from heat or toluene.

Movie S5. Soft robot steers trajectory directly toward light.

Movie S6. “NOR” response.

Movie S7. “AND” response.

Movie S8. “XOR” response.

Movie S9. Autonomous motion of soft robot with multiple control modules.

Movie S10. Soft robot autonomously changes its trajectory.

REFERENCES AND NOTES

1. C. Majidi, Soft robotics: A perspective–Current trends and prospects for the future. *Soft Robot.* **1**, 5–11 (2014).
2. D. Rus, M. T. Tolley, Design, fabrication and control of soft robots. *Nature* **521**, 467–475 (2015).
3. C. Laschi, M. Cianchetti, B. Mazzolai, L. Margheri, M. Follador, P. Dario, Soft robot arm inspired by the octopus. *Adv. Robot.* **26**, 709–727 (2012).
4. R. F. Shepherd, F. Ilievski, W. Choi, S. A. Morin, A. A. Stokes, A. D. Mazzeo, X. Chen, M. Wang, G. M. Whitesides, Multigait soft robot. *Proc. Natl. Acad. Sci. U.S.A.* **108**, 20400–20403 (2011).
5. M. Cianchetti, C. Laschi, A. Menciassi, P. Dario, Biomedical applications of soft robotics. *Nat. Rev. Mater.* **3**, 143–153 (2018).
6. H. Zhao, K. O'Brien, S. Li, R. F. Shepherd, Optoelectronically innervated soft prosthetic hand via stretchable optical waveguides. *Sci. Robot.* **1**, eaai7529 (2016).
7. M. Ishida, D. Drotman, B. Shih, M. Hermes, M. Luhar, M. T. Tolley, Morphing structure for changing hydrodynamic characteristics of a soft underwater walking robot. *IEEE Robot. Autom. Lett.* **4**, 4163–4169 (2019).
8. A. Kotikian, C. McMahan, E. C. Davidson, J. M. Muhammad, R. D. Weeks, C. Daraio, J. A Lewis, Untethered soft robotic matter with passive control of shape morphing and propulsion. *Sci. Robot.* **4**, eaax7044 (2019).
9. C. D. Onal, D. Rus, Autonomous undulatory serpentine locomotion utilizing body dynamics of a fluidic soft robot. *Bioinspir. Biomim.* **8**, 026003 (2013).
10. T. Kalisky, Y. Wang, B. Shih, D. Drotman, S. Jadhav, E. Aronoff-Spencer, M. T. Tolley, Differential pressure control of 3D printed soft fluidic actuators, in *2017 IEEE/RSJ International Conference on Intelligent Robots and Systems (IROS)*, (IEEE, 2017), pp. 6207–6213.
11. Y. Wu, J. K. Yim, J. Liang, Z. Shao, M. Qi, J. Zhong, Z. Luo, X. Yan, M. Zhang, X. Wang, R. S. Fearing, R. J. Full, L. Lin, Insect-scale fast moving and ultrarobust soft robot. *Sci. Robot.* **4**, eaax1594 (2019).
12. Z. Wang, K. Li, Q. He, S. Cai, A light-powered ultralight tensegrity robot with high deformability and load capacity. *Adv. Mater.* **31**, 1806849 (2019).
13. M. T. Tolley, R. F. Shepherd, B. Mosadegh, K. C. Galloway, M. Wehner, M. Karpelson, R. J. Wood, G. M. Whitesides, A resilient, untethered soft robot. *Soft Robot.* **1**, 213–223 (2014).

14. H. Yuk, S. Lin, C. Ma, M. Takaffoli, N. X. Fang, X. Zhao, Hydraulic hydrogel actuators and robots optically and sonically camouflaged in water. *Nat. Commun.* **8**, 14230 (2017).

15. Y. Chi, Y. Hong, Y. Zhao, Y. Li, J. Yin, Snapping for high-speed and high-efficient butterfly stroke–Like soft swimmer. *Sci. Adv.* **8**, eadd3788 (2022).

16. X. Ji, X. Liu, V. Cacucciolo, M. Imboden, Y. Civet, A. E. Haitami, S. Cantin, Y. Perriard, H. Shea, An autonomous untethered fast soft robotic insect driven by low-voltage dielectric elastomer actuators. *Sci. Robot.* **4**, eaaz6451 (2019).

17. E. Acome, S. K. Mitchell, T. G. Morrissey, M. B. Emmett, C. Benjamin, M. King, M. Radakovitz, C. Keplinger, Hydraulically amplified self-healing electrostatic actuators with muscle-like performance. *Science* **359**, 61–65 (2018).

18. Q. He, Z. Wang, Y. Wang, A. Minori, M. T. Tolley, S. Cai, Electrically controlled liquid crystal elastomer–Based soft tubular actuator with multimodal actuation. *Sci. Adv.* **5**, eaax5746 (2019).

19. Q. He, Z. Wang, Y. Wang, Z. Wang, C. Li, R. Annapooranan, J. Zeng, R. Chen, S. Cai, Electrospun liquid crystal elastomer microfiber actuator. *Sci. Robot.* **6**, eabi9704 (2021).

20. Y. Zhao, Y. Hong, F. Qi, Y. Chi, H. Su, J. Yin, Self-sustained snapping drives autonomous dancing and motion in free-standing wavy rings. *Adv. Mater.* **35**, e2207372 (2023).

21. Q. Ze, X. Kuang, S. Wu, J. Wong, S. M. Montgomery, R. Zhang, J. M. Kovitz, F. Yang, H. J. Qi, R. Zhao, Magnetic shape memory polymers with integrated multifunctional shape manipulation. *Adv. Mater.* **32**, 1906657 (2020).

22. Y. Kim, H. Yuk, R. Zhao, S. A. Chester, X. Zhao, Printing ferromagnetic domains for untethered fast-transforming soft materials. *Nature* **558**, 274–279 (2018).

23. Y. Zhao, C. Xuan, X. Qian, Y. Alsaid, M. Hua, L. Jin, X. He, Soft phototactic swimmer based on self-sustained hydrogel oscillator. *Sci. Robot.* **4**, eaax7112 (2019).

24. Y. Zhao, C.-Y. Lo, L. Ruan, C.-H. Pi, C. Kim, Y. Alsaid, I. Frenkel, R. Rico, T.-C. Tsao, X. He, Somatosensory actuator based on stretchable conductive photothermally responsive hydrogel. *Sci. Robot.* **6**, eabd5483 (2021).

25. E. Brown, N. Rodenberg, J. Amend, A. Mozeika, E. Steltz, M. R. Zakin, H. Lipson, H. M. Jaeger, Universal robotic gripper based on the jamming of granular material. *Proc. Natl. Acad. Sci. U.S.A.* **107**, 18809–18814 (2010).

26. F. Ilievski, A. D. Mazzeo, R. F. Shepherd, X. Chen, G. M. Whitesides*,* Soft robotics for chemists. *Angew. Chem. Int. Ed. Engl.* **50**, 1890–1895 (2011).

27. C. Wang, K. Sim, J. Chen, H. Kim, Z. Rao, Y. Li, W. Chen, J. Song, R. Verduzco, C. Yu, Soft ultrathin electronics innervated adaptive fully soft robots. *Adv. Mater.* **30**, 1706695 (2018).

28. Y. Tang, Y. Chi, J. Sun, T.H. Huang, O. H. Maghsoudi, A. Spence, J. Zhao, H. Su, J. Yin, Leveraging elastic instabilities for amplified performance: Spine-inspired high-speed and high-force soft robots. *Sci. Adv.* **6**, eaaz6912 (2020).

29. Y. Kim, J. van den Berg, A. J. Crosby, Autonomous snapping and jumping polymer gels. *Nat. Mater.* **20**, 1695–1701 (2021).

30. N. W. Bartlett, M. T. Tolley, J. T. B. Overvelde, J. C. Weaver, B. Mosadegh, K. Bertoldi, G. M. Whitesides, R. J. Wood, A 3D-printed, functionally graded soft robot powered by combustion. *Science* **349**, 161–165 (2015).

31. J. H. Pikul, S. Li, H. Bai, R. T. Hanlon, I. Cohen, R. F. Shepherd, Stretchable surfaces with programmable 3D texture morphing for synthetic camouflaging skins. *Science* **358**, 210–214 (2017).

32. E. Siéfert, E. Reyssat, J. Bico, B. Roman, Bio-inspired pneumatic shape-morphing elastomers. *Nat. Mater.* **18**, 24–28 (2019).

33. T. G. Thuruthel, B. Shih, C. Laschi, M. T. Tolley, Soft robot perception using embedded soft sensors and recurrent neural networks. *Sci. Robot.* **4**, eaav1488 (2019).

34. K. Y. Ma, P. Chirarattananon, S. B. Fuller, R. J. Wood, Controlled flight of a biologically inspired, insect-scale robot. *Science* **340**, 603–607 (2013).

35. Z. Zhakypov, K. Mori, K. Hosoda, J. Paik, Designing minimal and scalable insect-inspired multi-locomotion millirobots. *Nature* **571**, 381–386 (2019).

36. J. Sauder, E. Hilgemann, J. Kawata, K. Stack, A. Parness, M. Johnson, Automation rover for extreme environments (aree). (2017).

37. H. Yasuda, P. R. Buskohl, A. Gillman, T. D. Murphey, S. Stepney, R. A. Vaia, J. R. Raney, Mechanical computing. *Nature* **598**, 39–48 (2021).

38. M. Sitti, Physical intelligence as a new paradigm. *Extreme Mech. Lett.* **46**, 101340 (2021).

39. M. Wehner, R. L. Truby, D. J. Fitzgerald, B. Mosadegh, G. M. Whitesides, J. A. Lewis, R. J. Wood, An integrated design and fabrication strategy for entirely soft, autonomous robots. *Nature* **536**, 451–455 (2016).

40. Y. Zhao, Y. Chi, Y. Hong, Y. Li, S. Yang, J.Yin, Twisting for soft intelligent autonomous robot in unstructured environments. *Proc. Natl. Acad. Sci. U.S.A.* **119**, e2200265119 (2022).

41. H. Cui, D. Yao, R. Hensleigh, H. Lu, A. Calderon, Z. Xu, S. Davaria, Z. Wang, P. Mercier, P. Tarazaga, X. R. Zheng, Design and printing of proprioceptive three-dimensional architected robotic metamaterials. *Science* **376**, 1287–1293 (2022).
42. D. Drotman, S. Jadhav, D. Sharp, C. Chan, M. T. Tolley, Electronics-free pneumatic circuits for controlling soft-legged robots. *Sci. Robot.* **6**, eaay2627 (2021).
43. P. Rothemund, A. Ainla, L. Belding, D. J. Preston, S. Kurihara, Z. Suo, G. M. Whitesides, A soft, bistable valve for autonomous control of soft actuators. *Sci. Robot.* **3**, eaar7986 (2018).
44. A. Rafsanjani, K. Bertoldi, A. R. Studart, Programming soft robots with flexible mechanical metamaterials. *Sci. Robot.* **4**, eaav7874 (2019).
45. K. Bertoldi, V. Vitelli, J. Christensen, M. van Hecke, Flexible mechanical metamaterials. *Nat. Rev. Mater.* **2**, 17066 (2017).
46. H. Yasuda, T. Tachi, M. Lee, J. Yang, Origami-based tunable truss structures for non-volatile mechanical memory operation. *Nat. Commun.* **8**,962 (2017).
47. T. Mei, Z. Meng, K. Zhao, C. Q. Chen, A mechanical metamaterial with reprogrammable logical functions. *Nat. Commun.* **12**, 7234 2021.
48. B. Treml, A. Gillman, P. Buskohl, R. Vaia, Origami mechanologic. *Proc. Natl. Acad. Sci. U.S.A.* **115**, 6916–6921 2018.
49. Y. Hong, Y. Chi, S. Wu, Y. Li, Y. Zhu, J. Yin, Boundary curvature guided programmable shape-morphing kirigami sheets. *Nat. Commun.* **13**, 530 2022.
50. Y. Li, Q. Zhang, Y. Hong, J. Yin, 3D transformable modular kirigami based programmable metamaterials. *Adv. Funct. Mater.* **31**, 2105641 2021.
51. Y. Jiang, L. M. Korpas, J. R. Raney, Bifurcation-based embodied logic and autonomous actuation. *Nat. Commun.* **10**, 128 2019.
52. L. M. Korpas, R. Yin, H. Yasuda, J. R. Raney, Temperature-responsive multistable metamaterials. *ACS Appl. Mater. Interfaces* **13**, 31163–31170 2021.
53. J. N. Grima, K. E. Evans, Auxetic behavior from rotating squares. *J. Mater. Sci. Lett.* **19**, 1563–1565 (2000).
54. B. Deng, J. R. Raney, V. Tournat, K. Bertoldi, Elastic vector solitons in soft architected materials. *Phys. Rev. Lett.* **118**, 204102 2017.
55. B. Deng, C. Mo, V. Tournat, K. Bertoldi, J. R. Raney, Focusing and mode separation of elastic vector solitons in a 2D soft mechanical metamaterial. *Phys. Rev. Lett.* **123**, 024101 2019.

56. H. Yasuda, L. M. Korpas, J. R. Raney, Transition waves and formation of domain walls in multistable mechanical metamaterials. *Phys. Rev. Appl.* **13**, 054067 (2020).
57. C. Ahn, X. Liang, S. Cai, Inhomogeneous stretch induced patterning of molecular orientation in liquid crystal elastomers. *Extreme Mech. Lett.* **5**, 30–36 2015.
58. J. M. Boothby, T. H. Ware, Dual-responsive, shape-switching bilayers enabled by liquid crystal elastomers. *Soft Matter* **13**, 4349–4356 2017.
59. Y. Shang, J. Liu, M. Zhang, W. He, X. Cao, J. Wang, T. Ikeda, L. Jiang, Reversible solvent-sensitive actuator with continuous bending/debending process from liquid crystal elastomer-colloidal material. *Soft Matter* **14**, 5547–5553 2018.
60. C. Yang, F. Su, Y. Xu, Y. Ma, L. Tang, N. Zhou, E. Liang, G. Wang, J. Tang, pH oscillator-driven jellyfish-like hydrogel actuator with dissipative synergy between deformation and fluorescence color change. *ACS Macro Lett.* **11**, 347–353 2022.
61. Z. Wang, W. Fan, Q. He, Y. Wang, X. Liang, S. Cai, A simple and robust way towards reversible mechanochromism: Using liquid crystal elastomer as a mask. *Extreme Mech. Lett.* **11**, 42–48 2017.
62. F. Connolly, P. Polygerinos, C. J. Walsh, K. Bertoldi, Mechanical programming of soft actuators by varying fiber angle. *Soft Robot.* **2**, 26–32 2015.
63. C. M. Yakacki, M. Saed, D. P. Nair, T. Gong, S. M. Reed, C. N. Bowman, Tailorable and programmable liquid-crystalline elastomers using a two-stage thiol-acrylate reaction. *RSC Adv.* **5**, 18997–19001 (2015).
64. J.-Y. Sun, X. Zhao, W. R. K. Illeperuma, O. Chaudhuri, K. H. Oh, D. J. Mooney, J. J. Vlassak, Z. Suo, Highly stretchable and tough hydrogels. *Nature* **489**, 133–136 (2012).
65. Q. He, Z. Wang, Y. Yan, J. Zheng, S. Cai, Polymer nanofiber reinforced double network gel composite: Strong, tough and transparent. *Extreme Mech. Lett.* **9**, 165–170 (2016).
66. S. Y. Kim, R. Baines, J. Booth, N. Vasios, K. Bertoldi, R. Kramer-Bottiglio, Reconfigurable soft body trajectories using unidirectionally stretchable composite laminae. *Nat. Commun.* **10**, 3464 (2019).
67. P. Polygerinos, P. Polygerinos, S. Lyne, Z. Wang, L. F. Nicolini, B. Mosadegh, G. M. Whitesides, C. J. Walsh, Towards a soft pneumatic glove for hand rehabilitation, *IEEE/RSJ International Conference on Intelligent Robots and Systems* , second of two volume second of two pages 1512–1517 (second of two year 2013). bibitem Stop